

Bizonal cardiac engineered tissues with differential maturation features in a mid-throughput multimodal bioreactor

*Original*

Bizonal cardiac engineered tissues with differential maturation features in a mid-throughput multimodal bioreactor / Pisanu, Alessia; Reid, Gregory; Fusco, Deborah; Sileo, Antonio; Robles Diaz, Diana; Tarhini, Hadi; Putame, Giovanni; Massai, DIANA NADA CATERINA; Isu, Giuseppe; Marsano, Anna. - In: ISCIENCE. - ISSN 2589-0042. - (2022). [10.1016/j.isci.2022.104297]

*Availability:*

This version is available at: 11583/2963938 since: 2022-05-17T15:00:23Z

*Publisher:*

Elsevier

*Published*

DOI:10.1016/j.isci.2022.104297

*Terms of use:*

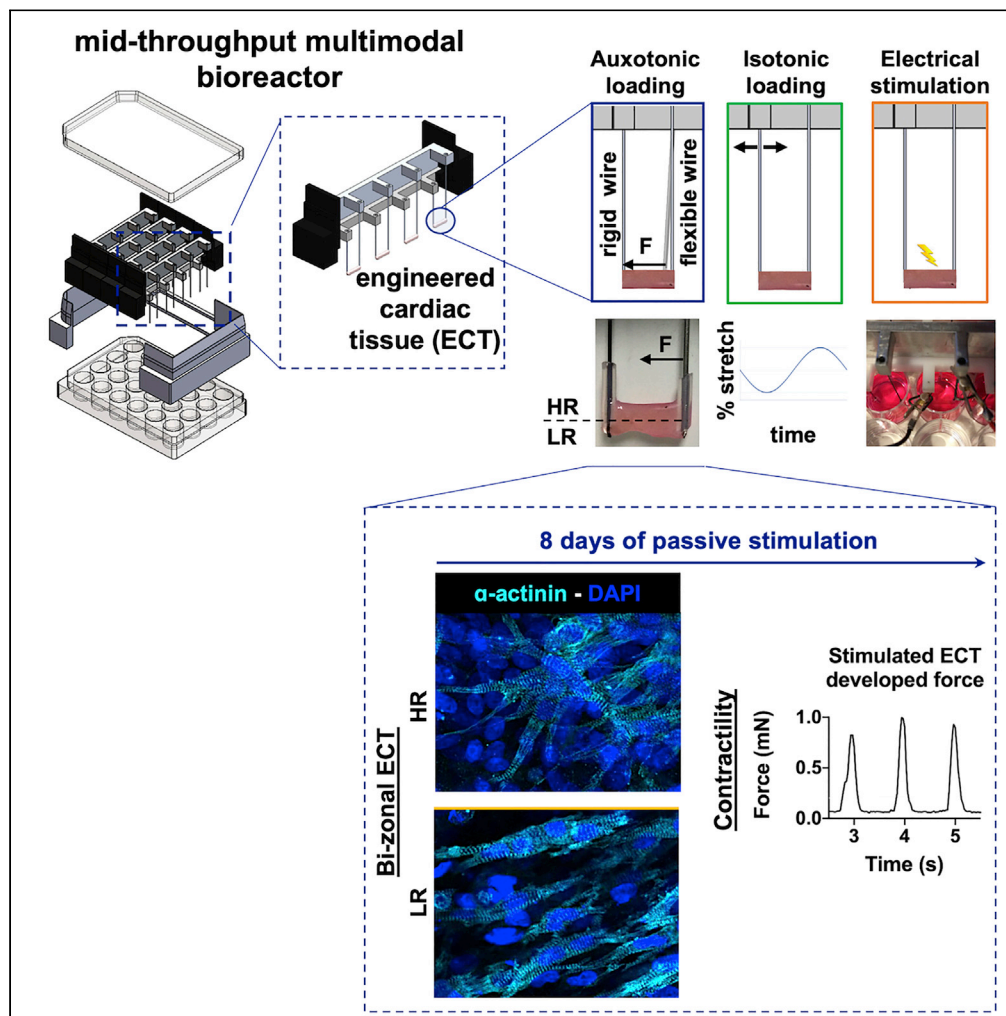
This article is made available under terms and conditions as specified in the corresponding bibliographic description in the repository

*Publisher copyright*

(Article begins on next page)

## Article

# Bizonal cardiac engineered tissues with differential maturation features in a mid-throughput multimodal bioreactor



Alessia Pisanu,  
Gregory Reid,  
Deborah Fusco, ...,  
Diana Massai,  
Giuseppe Isu,  
Anna Marsano

anna.marsano@usb.ch

## Highlights

Mid-throughput culture platform to engineer reproducible 3D cardiac *in vitro* models

3D culture under multiphysical stimuli mimicking the *in vivo* heart environment

Passive loading leads to bizonal constructs with different cardiac maturation stages

Pisanu et al., iScience 25, 104297  
May 20, 2022 © 2022 The Authors.  
<https://doi.org/10.1016/j.isci.2022.104297>

## Article

## Bizonal cardiac engineered tissues with differential maturation features in a mid-throughput multimodal bioreactor

Alessia Pisanu,<sup>1,2</sup> Gregory Reid,<sup>1,2</sup> Deborah Fusco,<sup>1,2</sup> Antonio Sileo,<sup>1,2</sup> Diana Robles Diaz,<sup>1,2</sup> Hadi Tarhini,<sup>3</sup> Giovanni Putame,<sup>3</sup> Diana Massai,<sup>3</sup> Giuseppe Isu,<sup>1,2,4</sup> and Anna Marsano<sup>1,2,4,5,\*</sup>

## SUMMARY

**Functional three-dimensional (3D) engineered cardiac tissue (ECT) models are essential for effective drug screening and biological studies. Application of physiological cues mimicking those typical of the native myocardium is known to promote the cardiac maturation and functionality *in vitro*. Commercially available bioreactors can apply one physical force type at a time and often in a restricted loading range. To overcome these limitations, a millimetric-scale microscope-integrated bioreactor was developed to deliver multiple biophysical stimuli to ECTs. In this study, we showed that the single application of auxotonic loading (passive) generated a bizonal ECT with a unique cardiac maturation pattern. Throughout the statically cultured constructs and in the ECT region exposed to high passive loading, cardiomyocytes predominantly displayed a round morphology and poor contractility ability. The ECT region with a low passive mechanical stimulation instead showed both rat- and human-origin cardiac cell maturation and organization, as well as increased ECT functionality.**

## INTRODUCTION

Traditional *in vitro* models for investigating cardiotoxicity rely mostly on monolayer cultures of noncardiac cells, such as human embryonic kidney (HEK) cells, transduced with cardiac-muscle-related ion channels (Eschenhagen and Zimmermann, 2005; Lu et al., 2015; Wright et al., 2020). Recently, newly developed three-dimensional (3D) models use clinically relevant human-derived cardiomyocytes (Dostanic et al., 2019; Thavandiran et al., 2020), but they still often lack the complexity of *in vivo* cardiac tissue organization. 3D cardiac tissue models with a high degree of maturation are therefore preferable to improve drug candidate selection as well as to elucidate key morphogenetic and remodeling events occurring during cardiac development and pathophysiology (Griffith and Swartz, 2006; Hinson et al., 2015; Nugraha et al., 2019). Bio-mimetic approaches known to promote maturation (Karbassi et al., 2020) of 3D engineered cardiac tissues (ECTs) typically provide during *in vitro* culture some of the key aspects of the multicellular and multibiophysical microenvironment typical of native heart tissue (Goldfracht et al., 2019; Veldhuizen et al., 2019; Zuppinger, 2019). Among the several cardiac biophysical cues investigated, mechanical stimulation was demonstrated to strongly improve cardiomyocyte organization and maturation in ECTs (Zimmermann et al., 2002; Massai et al., 2013; Liaw and Zimmermann, 2016; Stoppel et al., 2016). Many protocols have been implemented to generate mechanically stimulated ECTs, applying different loading conditions: static load (isometric contraction); the most commonly used active phasic load (isotonic contraction); and passive auxotonic stimulation upon flexible load (Liaw and Zimmermann, 2016). Isotonic loading is a defined active cyclical stretch usually applied to ECTs following few days of static preculture (Kensah et al., 2011; Morgan and Black, 2014; Lux et al., 2016). It is appropriate for engineered constructs at an advanced stage of maturation due to the imposition of an active acute loading regime (e.g. Boudou et al., 2012). On the contrary, auxotonic stimulation is a passive physiological loading condition applied by using flexible posts, which allow cardiomyocytes to develop a passive force and start pulling. Therefore, auxotonic stimulation seems appropriate for cardiac tissues in early development stage, as the load progressively adapts to the maturation of the cardiomyocytes. Either auxotonic or isotonic mechanical stimulations are adopted to promote the development of functional ECTs *in vitro* (Eschenhagen et al., 1997; Zimmermann et al., 2002; Ye Morgan and Black, 2014) at a large- or micro-scale. Micro-physiological devices are desirable for the high-throughput screening opportunity (Marsano et al., 2016; Visone et al., 2016; Costa et al., 2020). However,

<sup>1</sup>Department of Biomedicine, University of Basel, Hebelstrasse 20, 4031 Basel, Switzerland

<sup>2</sup>Department of Surgery, University Hospital of Basel, Hebelstrasse 20, 4031 Basel, Switzerland

<sup>3</sup>PolitoBIOMed Lab, Department of Mechanical and Aerospace Engineering, Politecnico di Torino, Turin, Italy

<sup>4</sup>These authors contributed equally

<sup>5</sup>Lead contact

\*Correspondence: anna.marsano@usb.ch  
<https://doi.org/10.1016/j.isci.2022.104297>



such systems often do not allow the simultaneous controlled application of different types and ranges of loading as well as a reliable monitoring and assessment of the ECT functionality in real time (Mittal et al., 2019). On the contrary, the generation of macro-scale ECTs allows for applying a more reliable large-range mechanical stimulation and performing multiple ECT's assessments (Kensah et al., 2011; Massai et al., 2020). However, such devices usually consist of quite complex, bulky structures with a low-throughput capability and without live-imaging compatibility. Models at the millimeter scale (mm-scale) offer instead the possibility to apply wider types and ranges of loading and to analyze a larger number of key ECT parameters in a high-throughput manner (Dostanic et al., 2019; Zhao et al., 2019a, 2019b; Thavandiran et al., 2020). With the ultimate goal of generating a functional and reproducible (mm-scale) ECT 3D model allowing medium-/high-throughput assays and live-imaging monitoring, we designed a novel multimodal microscope-integrated bioreactor to incorporate for the first time two different types of mechanical loading (auxotonic and isotonic) and electrical stimulation in the same device. In this study, we characterized each single module of the bioreactor and focused on investigating the role of flexible passive load on the ECT functionality generated with either neonatal-rat- or human-induced pluripotent stem-cell-derived (hiPSC-CMs) cardiomyocytes.

## RESULTS

### Bioreactor design and characterization

The design of the developed bioreactor for mm-scale ECTs allowed a reproducible and user-friendly generation of 24 independent constructs and culture in a multiphysical environment (Figures 1A–1D), thanks to a compact set-up, fitting to a standard 24-well plastic culture plate (Figure S1A). The imaging compatibility with most common microscope systems gave this unique structure the possibility to perform nondestructive monitoring as well as to be modular and versatile (Figures S1B and S1C). Moreover, for the first time a bioreactor combined active and passive loading regimes as well as electrical stimulation (Ronaldson-Bouchard et al., 2019). The main advantage of the proposed design was the use of two conductive wires, one rigid (made of stainless-steel) and the other flexible (nitinol) to embed hydrogel-based ECTs directly in the bioreactor's stimulation modules (Figure 1D and 1E), to apply the isotonic and auxotonic loadings (exploiting the rigid and flexible wire, respectively) as well as the electrical stimulation (Figure 1F). Cycling stretching was achieved connecting an electrical stepper motor (or a controlled syringe pump) to the mechanical stimulation module and cyclically displacing the rigid stainless-steel wire. Both mechanical and electrical stimulations were characterized and validated as functional and reproducible in the interested working range (Figure S2). Real-time imaging of the flexible wire displacement worked as sensor to measure *in-situ* force of contraction. In particular, the adopted nitinol wire had a calibrated stiffness of 12 mN/mm, allowing to measure contraction forces in the range of 0.1–10 mN simply detecting wire-tip displacements under ECT contractions (Figure S2B). This force range covered the properties of engineered muscle tissues (Eschenhagen and Zimmermann, 2005; Ribeiro et al., 2019). The higher was the stiffness of the nitinol wire (i.e. controlling nitinol wire diameter) and the range of force detectable by the read of wire displacement, also permitting to tune and model different levels of physiopathological conditions. To characterize the active stimulation module, different cyclic strains were tested at a physiological range of frequencies (1–3 Hz). The comparisons between measured displacement of the motor shaft and ideal motion waveform (Figure S2C) showed mean percentage errors between measured and nominal stretching amplitude values ranging from  $4.22\% \pm 0.51\%$  to  $1.95\% \pm 0.14\%$  (Figure S2D). The mean percentage errors between measured and nominal frequency values were instead generally negligible, with the only exception of 0.097% for the combination strain-frequency of 0.8 mm–3 Hz (Figure S2E). However, at the highest tested frequency (3 Hz), it was possible to apply only a 0.8 mm strain.

The finite element modelling of the electric field in the culture chambers described the 3D pattern of the electric field and current density throughout the different parts of the construct for an ECT length equal to 8 mm (Table 1). The current density graph (Figure S2F), in which the volume arrows indicated its direction and distribution, showed that the construct was entirely stimulated by a current flow perpendicular to the electrode surface. Moreover, based on the representation of the electric field amplitude (Figure S2G), it was possible to observe that the presence of the PDMS supports avoided to expose the construct directly in contact with the electrodes to high voltages. The color map displayed that the whole construct was subject to an electric field amplitude lower than 2 V/cm when the stimulator was imposed to a value of 5 V. When the electrical field was measured along the axis of the construct (Figure S2H), the values were uniform throughout the whole length of the construct and resulted to be around 1.1 V/cm (5 times lower than the 5 V set as potential).

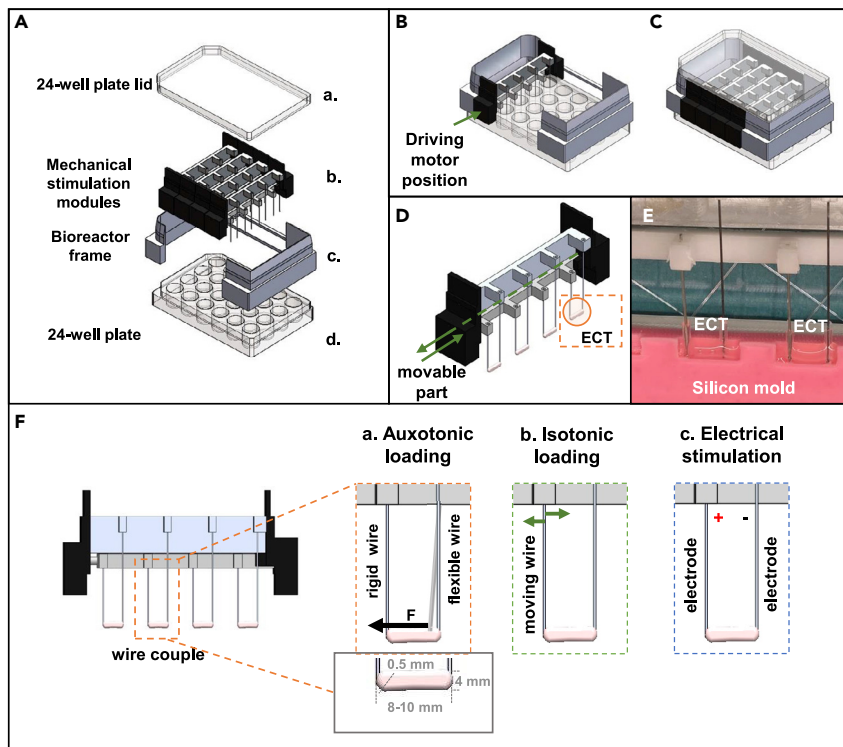


**Figure 1. Bioreactor design**

(A) Representation of the modular bioreactor incorporated with 24-well culture plates.

The 3D printed bioreactor frame (c.) is placed between the 24-well plate (d.) and the lid (a.). It is possible to combine 6 independent mechanical stimulation modules (b.), allowing independent mechanical stimulation of 4 separate culture well rows (B and C).

(D) Representation of ECTs cast in between 2 metal wires of the mechanical stimulation module.

(E) Images of the cell-based fibrin gel generation in custom-made silicon mold.

(F) Bioreactor's modules functioning scheme: flexible wires provide resistance during auxotonic contraction and serve as sensors for measuring the contractile force  $F$  (a.); rigid wires are fixed in a moving shaft, connected to a driving stepper motor for delivery of active cyclical stretching (b.); the wire couple in between which the ECT is generated are used as conductive electrodes and connected to an electrical stimulator for application of electrical stimuli (c.).

The electrical characterization also showed that the injected charge, carried out by the ions inside the culture medium in which the constructs were kept during the electrical pacing, produced the electrical field to which the tissue was exposed to and was then almost totally recovered (nonfaradaic charging/discharging mechanism) (Figures S2I–S2K). That balance between the injected and the recovered charge confirmed that the electrical stimuli did not produce by-products that could be harmful for the cells (Tandon et al., 2009).

### Auxotonic stimulation improved the cardiac maturation in rat origin ECTs

In all the experimental conditions, neonatal-rat-derived cardiac cells were overall spatially uniformly distributed throughout the hydrogel. In statically cultured tissues, most of the cardiac sarcomeric  $\alpha$ -actinin-positive cells displayed a round morphology, typical of *in vitro* nonmature CMs. Only few CMs displayed sarcomeric units with a primitive organization (Figure 2A: Control). On the contrary, in passively stimulated ECTs, overall most of the CMs showed the typical rod-shaped morphology of adult phenotype with mature sarcomere structure (Hirt et al., 2014) (Figure 2A: Stimulated). Image analyses also showed that the area positive for cardiac sarcomeric  $\alpha$ -actinin was superior in stimulated ECTs and confirmed that CMs were more elongated and aligned toward the load direction compared with static condition (Figure 2B). Moreover, the sarcomeric unit in stimulated CMs possessed a significantly higher length ( $0.7 \pm 0.57 \mu\text{m}$ ) compared with the static cultured ECTs ( $0.2 \pm 0.35 \mu\text{m}$ ) (Figure 2B), similar to the one known for adult CM unit (in average  $2.2 \mu\text{m}$ , Yuxuan and Pu, 2020). However, in stimulated ECT cardiac maturation was not uniform, but varied depending on the region of the ECTs. In this regard, two distinct regions were

**Table 1. Characterization of the electrical module**

Material parameters	PS	PDMS	Medium	Nitinol	Stainless steel 316	Fibrin-gel
Electrical conductivity (S/m)	$6.7e^{-14}$	$0.83e^{-12}$	1.5	1320000	1351351	1.5
Relative permittivity	3	2.69	80	1	1	80

Electrical material parameters of the main elements composing the bioreactor's electrical stimulation module.

identified in stimulated ECTs, corresponding to two different heights of the flexible cantilever. At these two points of the cantilever there were two different beam bending moments and, therefore, two different stiffness resulting in a low- (LR) and a high- (HR) resistance zone (Figure 2C). The difference in deformation strain between HR and LR zones calculated using the beam elastic curve equation (STAR Methods) was estimated to be approximately of 17%.

Proper CM morphology, elongation and orientation, as well as sarcomere organization with clear Z-band striations were observed exclusively in the LR regions (Figure 2D). In the HR regions instead CMs predominantly showed a round cell morphology and a lower sarcomere organization similar to control constructs (Figure 2D). The cardiomyocyte ultrastructure was also investigated using transmission electron microscopy (TEM) (Figure 2E). In the stimulated tissues, the mitochondria (M) were overall completely formed with high-density cristae structure and bigger in size compared with control constructs (Figure 2E-f.). In the control ECTs, instead, mitochondria were in an early stage of development (Figure 2E-a.) and the sarcomeres structure (S) were not defined yet (Figure 2E-c.). Spatial differences in the cell organelle structures in the two different portions of the stimulated tissue were observed. However, we observed that only in the low-resistance zone (LR), Z-lines (Figure 2E-h.) and primitive structure of desmosomes (Figure 2E-i.) were present. Furthermore, image analysis confirmed that in the LR regions of stimulated ECTs, CMs had an elevated length to width ratio and were mainly aligned in the direction of the imposed passive force (Figure 2F). Further assessment of CM elongation and maturation included the quantification of CM length, length-width ratio, as well as sarcomere length, which resulted to be  $26 \pm 10 \mu\text{m}$ ,  $2 \pm 0.4$ , and  $1.1 \pm 0.2 \mu\text{m}$  and  $17.8 \pm 4.3 \mu\text{m}$ ,  $1.6 \pm 0.2$ , and  $0.5 \pm 0.4 \mu\text{m}$  for stimulated and static conditions, respectively (Figure 2F). However, if only stimulated CMs from the LR region were taken into consideration, CM average length rose up to  $38.4 \pm 8 \mu\text{m}$  and the length-to-width ratio increased up to 2.5 user defined metric (udm, Figure 2F). CM alignment was also quantified, showing that in stimulated constructs the majority of CMs were aligned in one direction (in case of auxotonic loading: the direction of the imposed force), whereas in control ECTs, no preferential alignment direction was observed (Figures 2G and 2H).

### Typical adult cardiac cell markers were increased after auxotonic loading

The influence of auxotonic stimulation on the gene expression of both adult- and fetal-like cardiac markers was investigated performing real-time qPCR and compared with nonstimulated ECTs (Figure 3A). An increase of the expression of Connexin-43 (*Gaj1* 1.9-fold) and Troponin-I (*Tnni3*, 1.7-fold), although not statistically significant, was observed at the mRNA level in stimulated ECTs. At the protein level, Connexin-43 expression was 1.45-fold higher compared with the control (Figure S4). Moreover, passive stimulated ECTs showed a superior mRNA expression of adult CM markers such as myosin light chain 2 (*Myl2*) and myosin heavy chain 6 (*Myh6*) compared with the control. On the contrary, myosin light chain 7 (*Myl7*), a typical cardiac fetal phenotype marker, was upregulated in statically cultured ECTs compared with the stimulated ones. However, expression of myosin heavy chain 7 (*Myh7*), a fetal cardiac hallmark, was statistically higher in stimulated construct compared with static control tissues.

In our study, passive mechanical stimulation also led to a superior mRNA expression of N-Cadherin (*Cdh2*) compared with the control. N-cadherin instead, is a component of adherent junctions, with an essential function in the mechanical and electrical coupling of adjacent CM (Kostetskii et al., 2005; Vite and Radice, 2014). In the protein level expression of N-Cadherin there was 1.25-fold increase compared with the expression in the statically cultured constructs (Figure S3D). Those values were also compared with the gene expression level of the mentioned markers in the initial cardiac population used for the ECT generation (Figure 3B). Compared with the freshly isolated rat cardiac cells (day 0), an increase of the expression of *Tnni3* was observed after 8 days of auxotonic condition (1.3-fold). However, those results also revealed



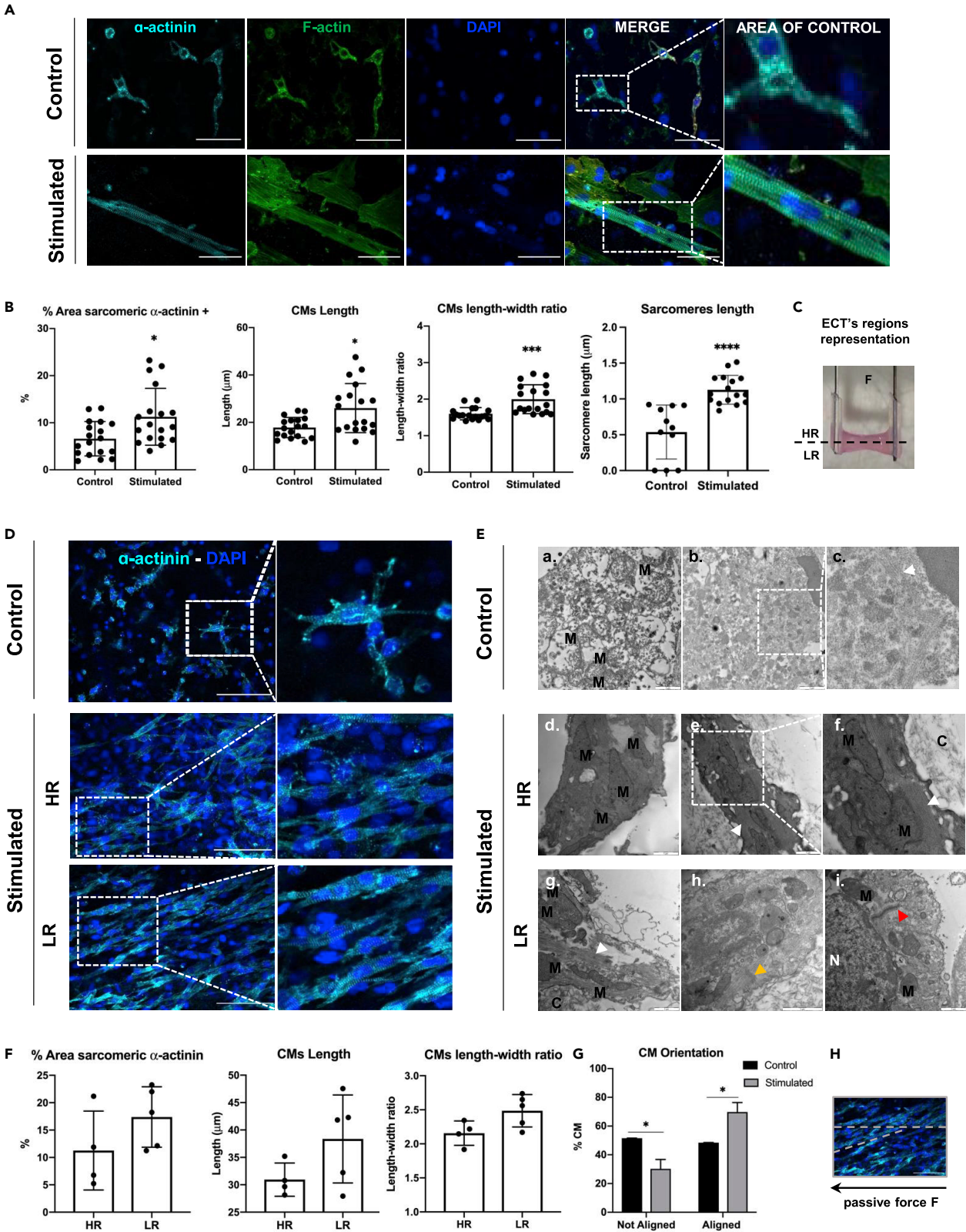


## Figure 2. ECTs cardiac maturation

(A) Representative immunofluorescence images of sarcomere organization in control ECTs and stimulated ECTs, stained for sarcomeric  $\alpha$ -actinin cardiac marker ( $\alpha$ -actinin, cyan), F-actin (F-actin, green). Nuclei were stained in blue (DAPI, blue). Area of control was identified for the sarcomere length quantification analysis. Scale bar: 50  $\mu$ m.

(B) Image-analysis-based quantification of sarcomeric  $\alpha$ -actinin positive area, cardiomyocytes (CMs) length and elongation ( $n = 2$ , from 2 independent experiments), and sarcomere length quantification ( $n = 2$ , from 3 independent experiments)  $*p \leq 0.05$ ;  $***p \leq 0.001$ ;  $****p \leq 0.0001$ .

(C) Schematic representation of the two identified zones within the stimulated ECTs: high resistance (HR) and low resistance (LR).

(D) Representative immunofluorescence images of statically cultured constructs and stimulated constructs, with a detailed view of low-resistance (LR) and high-resistance (HR) zones, stained for sarcomeric  $\alpha$ -actinin cardiac marker ( $\alpha$ -actinin, cyan). Nuclei were stained in blue (DAPI, blue). Scale bar: 100  $\mu$ m.

(E) Representative images of cardiomyocyte structures in control and stimulated tissues (HR and LR portion) acquired using transmission electron microscopy (TEM) technique. Mitochondria were indicated with M letter, nuclei with N, and the surrounding construct with C. White arrow heads pointed the sarcomeric myofibrils and yellow ones pointed Z-line, whereas red arrow heads indicated primitive desmosome structures. Scale bar: 1  $\mu$ m.

(F) Image-analysis-based quantification of sarcomeric  $\alpha$ -actinin positive area, cardiomyocytes (CMs) length and elongation for the two zones within the stimulated ECTs;  $n = 2$ , from 1 independent experiment.

(G) Graphical representation of the cardiomyocyte orientation within the tissue for statically cultured ECTs and stimulated ECTs ( $n = 2$ , from 2 independent experiments,  $*p \leq 0.05$ ) and schematic representation of the CMs alignment to the imposed passive force (H). Data were represented as mean  $\pm$  SD.

that on day 0 the expression of cardiac maturation hallmark, such as *Myl2*, was similar to the one after 8 days of either auxotonic or static culture. On the other hand, fetal-like markers, such as *Myl7* and *Myh7*, were more expressed in the freshly isolated cardiac population, as expected. Expression of *Myh6* remained instead superior in control tissues, also compared with the initial cardiac population (Figure 3B).

## ECT remodeling was superior under auxotonic stimulation

Stimulated ECTs were generated in a rectangular-like shape in a reproducible way by casting the cell-based fibrin gel into custom-made silicone molds (Figure 1E), and remodeling was observed following 8 days of culture (Figure 4A). A sand-timer-shaped cross section shrinking was observed throughout the culture at the center of stimulated ECTs (Figure 4B). H&E staining showed that in static condition (control) the cell-laden hydrogel had large voids, whereas in stimulated ECTs porous structures were mainly present only in the HR region. In contrast, the LR zone of stimulated ECTs was compact and remodeled (Figure 4C). The expression at the mRNA level of typical fibrosis markers was investigated (Figure 4D). In stimulated ECTs, expression of tenascin-C (*TnC*), collagen type I (*Col1a1*), and actin  $\alpha$ -2 (*Acta2*) was superior compared with control ECTs, whereas there was no difference in the expression of type 3 collagen (*Col3a1*) and matrix metalloproteinase (*Mmp9*) between the two experimental groups (Figure 4D). The expression of  $\alpha$  smooth muscle actin ( $\alpha$ -SMA) was also investigated, as it is usually expressed in not fully mature CMs or fibroblasts exposed to mechanical load (Bilyug, 2019). It was observed that  $\alpha$ -SMA was mainly expressed by CMs in static condition, confirming their lower degree of maturation (Bilyug, 2019), and by fibroblasts in dynamic condition (Figure 4E). Hypertrophic growth could be excluded for  $\alpha$ -SMA-expressing CMs in both experimental conditions, as the length and length-to-width ratio were both inferior to the values typical of adult normal phenotype. Proliferation marker (*Ki67*) expression was investigated in both statically and dynamically cultured ECTs with immunofluorescence staining. The *Ki67* expression was overall low expressed and mostly by cardiac  $\alpha$ -sarcomeric actinin negative cells (namely fibroblasts) in control constructs and in the HR zone of stimulated ECTs (Figure 4F).

## Auxotonic stimulation improved rat-origin ECT electrical functionality and force of contraction

Following 8 days of culture in either static or mechanical stimulation condition, ECTs response to an external electrical pacing was assessed to determine the functionality of the constructs. Fifty percent of the stimulated constructs demonstrated spontaneous beating without external pacing, whereas none of the static control tissues demonstrated this capability. The spontaneous contractions might be correlated to the presence of a pacemaker current and unstable resting membrane potential, both signs of a nonadult ventricular phenotype (Jiang et al., 2018). ECTs cultured under auxotonic conditions started to synchronously contract following an external pacing with significantly lower excitation threshold (ET, 10.4 times) compared with control constructs (Figure 5A). Nevertheless, the maximum tolerated beating frequency (maximum capture rate, MCR) was not different between the experimental groups (Figure 5B), but reached in both cases the normal rat heart frequency (around 3 Hz). In fact, once the statically cultured tissues reached the synchronous beating (excited with significantly higher electrical field compared with stimulated ECTs), they were able to follow in average the same imposed increasing pacing frequency of the stimulated constructs (Video S1. Response of a statically cultured ECT to an external electrical pacing, Video S2.



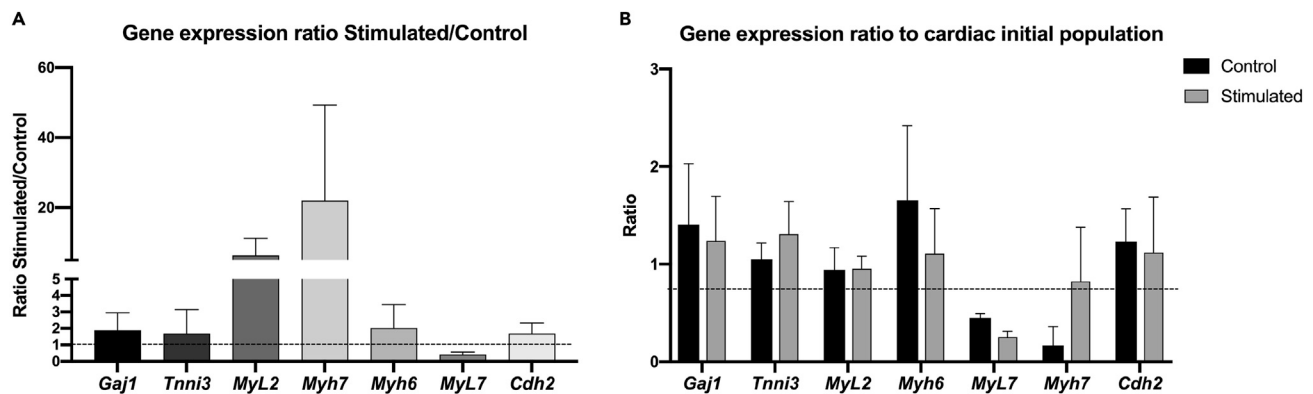


**Figure 3. Gene and protein expression analysis**

(A) mRNA expression ratio of stimulated ECTs versus statically cultured ECTs. n = 10, from 3 independent experiments.

(B) mRNA expression ratio of stimulated ECTs and statically cultured ECTs versus cardiac initial population. n = 4, from 1 independent experiment. Data were presented as mean  $\pm$  SEM.

Response of a ECT culture under passive stimulation to an external electrical pacing). In stimulated tissues, the flexible wire functioned as a cantilever (Video S3. Cantilever deflection upon electrical pacing of a ECT under passive) and allowed to quantify the force developed by ECTs upon electrical pacing. The cantilever bending was observed during the whole culture time and started to bend only from day 6. The maximum measured force of contraction was  $0.9 \pm 0.08$  mN (Figure 5C). Moreover, based on the strain contour map analysis, the mechanically stimulated ECTs were characterized by a greater and spatially more uniform deformation (Figure 5E) compared with the control samples (Figure 5D). Those qualitative results were confirmed by the quantification of the maximum median deformation (Figure 5G), which was significantly higher in stimulated ECTs compared with the control constructs.

### Auxotonic stimulation improved ECT maturation and functionality in hiPSC-based ECT

A mixed population of human CMs (18.3% expressing troponin-T by flow cytometry analysis) and hiPSCs committed to the cardiac lineage (progenitor cells) was used to generate the 3D constructs and investigate their distribution in the HR and LR regions. The presence of a bizonal maturation pattern was observed also in the human-origin cardiac cells. Similar to what was observed in the rat-origin ECTs, the hiPSC-derived CMs more advanced in the maturation were found in the LR portion, whereas most of the progenitor cardiac cells were confined in the HR region. As in rat-origin constructs, immunofluorescence staining displayed that in stimulated tissues cardiac  $\alpha$ -sarcomeric actinin-positive cells were aligned in the direction of the imposed passive force and showed a more mature sarcomere organization predominantly in the LR portion of the tissue. On the contrary, in the HR portion of the same stimulated ECTs, only few cells expressed sarcomeric  $\alpha$ -actinin and they displayed a round immature-like morphology (Figure 6A). In stimulated ECTs, hiPSCs showed to be all committed to the cardiac lineage, as they did not express OCT-4, a pluripotent marker for undifferentiated hiPSCs. hiPSCs resulted indeed positive either for Nkx2.5, an early transcription cardiac marker, or expressing late cardiac markers (namely alpha sarcomeric actinin) meaning that all hiPSCs were committed into either cardiac lineage or differentiated cardiomyocytes (Figure 6B). Moreover, although cardiac transcription factor Nkx2-5 was uniformly expressed by cells in the HR and LR regions, alpha sarcomeric actinin was almost exclusively expressed by cells in the LR region, confirming that LR load promoted cardiac differentiation (Figure 6B). The electrical functionality assessment showed that stimulated human ECTs showed a maximum external beating frequency (MCR) and an excitation threshold (contraction under electrical stimulation) similar to stimulated rat-origin ECTs (Figure 6C). Likewise, the force developed upon electrical pacing was measured using the flexible wire as a sensor; for the stimulated ECTs the maximum measured force of contraction was  $0.8 \pm 0.13$  mN (Figure 6D), similar to the value measured in rat-origin tissues ( $0.9 \pm 0.08$  mN).

### DISCUSSION

This study aimed to present a mid-/high-throughput bioreactor design with the unique feature to simultaneously apply passive, active mechanical loadings as well as electrical stimulation and to real-time monitor

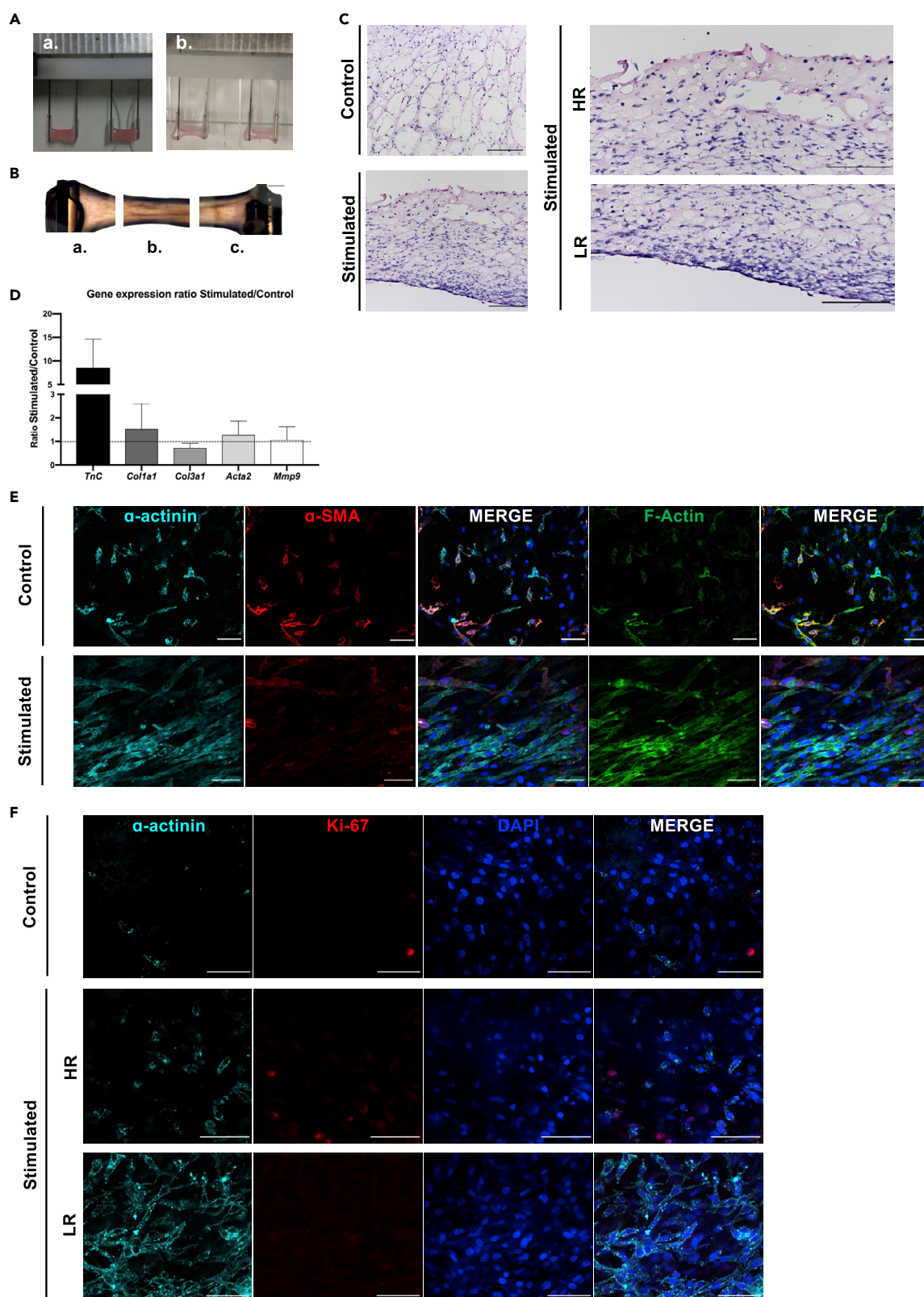


#### Figure 4. ECTs remodeling

(A) Images of ECTs at day 0 after cell-based fibrin gel generation (a.), and images of ECTs after 8 days of auxotonic stimulation (b.).  
 (B) Representative brightfield images of different portions of ECTs at day 8: fixed wire portion (a.), middle portion (b.), and flexible wire side (c.). Scale bar: 500  $\mu$ m.  
 (C) Representative H&E staining showing cell distribution and orientation within control ECT and stimulated ECTs, distinguishing between low- and high-resistance zones. Scale bar: 200  $\mu$ m.  
 (D) Fibrosis markers of mRNA expression represented with stimulated-to-control ratio.  
 (E) Representative immunofluorescence images of statically cultured ECT and stimulated ECTs stained for sarcomeric  $\alpha$ -actinin cardiac marker ( $\alpha$ -actinin, cyan) and  $\alpha$ -smooth muscle actin ( $\alpha$ -SMA, red). Nuclei were stained in blue (DAPI, blue). Scale bar: 50  $\mu$ m.  
 (F) Representative immunofluorescence images of statically cultured and stimulated ECTs, low-resistance (LR) and high-resistance (HR) zones, stained for sarcomeric  $\alpha$ -actinin cardiac marker ( $\alpha$ -actinin, cyan) and Ki67 (red). Nuclei were stained in blue (DAPI, blue). Scale bar: 50  $\mu$ m. Data were represented as mean  $\pm$  SEM.

the functionality of the ECTs. This tool was used here to investigate the effects of passive loading alone on CM maturation and organization. Our findings showed a superior differentiation stage of neonatal CM following passive loading compared with statically generated ECTs. Moreover, a spatially different pattern of cardiac maturation also within the same construct generated under passive loading was observed. Most likely, the observed differences in the maturation of CMs in the different zones might depend on a nonuniform exposition of the cells to the same mechanical load. Indeed, at the free edge (LR), the cantilever was more easily pulled by the cells compared with the cardiomyocytes attached to the flexible post at the opposite site (HR) experiencing a superior stiffness and therefore, a higher resistance. The fold of difference in the stiffness of the flexible post from one edge to the other corresponding to the height of the ECT was 1.35 (0.0059 and 0.0044 N/mm for the HR and LR sites of the cantilever).

In our experimental set-up, neonatal CMs did not yet acquire a fully mature adult phenotype, possibly due to the short culture period. Neonatal and adult phenotypes of CMs indeed differ in many aspects, including morphology, metabolism, and the expression and organization of adult-specific cardiac contractile proteins, as well as electrical and mechanical junctions and intracellular organelles. Adult cardiomyocytes possess highly organized and larger sarcomere units, as well as a high number of mitochondria with a complex network and elongated cristae structures providing enough energy sources for intense contractile activity (Hom et al., 2011; Zhao et al., 2019a, 2019b). In our study, several different aspects were analyzed to assess the level of cardiac maturation: cell morphology, ultra-structure organization, gene and protein expression as well as ECT functionality.

In rat ventricular CMs, the sarcomere unit is usually around 70  $\mu$ m long and has a length-to-width ratio of 3:1 (Oliver-Gelabert et al., 2020). In the present study, the CM length was inferior to that of adult ventricle CMs, although the stimulated CMs from the LR region showed values up to  $38.4 \pm 8 \mu$ m. Although the level of fully differentiated phenotype of adult cardiomyocytes was not yet achieved, the features of the cardiomyocytes in the LR of stimulated ECTs were encouraging considering that they were obtained with only 8 days of passive stimulation. A superior differentiation level of sarcomere units was achieved only when the culture reached 2–3 weeks (Leonard et al., 2018; Ronaldson et al., 2018; Veldhuizen et al., 2020). However, CM alignment and tissue organization was previously observed mainly using cyclical mechanical stimulation (Kensah et al., 2011; Lux et al., 2016; Massai et al., 2020), which provides the tissues with an active training leading to mature and organized tissues or with longer culture times than 8 days in culture under auxotonic stimulation (Zimmermann et al., 2002). In our experimental condition, the short time in culture and the exposure to a nonuniform auxotonic stimulation most likely allowed the formation of this bizonal pattern with unique differentiation features offering a relevant *in vitro* model to investigate the role of passive force in the differentiation and maturation process of CMs, as well as possible implications in the cardiac regeneration field. A possible strategy to expose the whole ECT to a uniform auxotonic stimulus could be to reduce the height of the construct or to increase the rigidity of the flexible post. However, both these two solutions might change the remodeling of the cardiac engineered tissue that could be either accelerated or further delayed, respectively.

Our findings demonstrated that most of cardiac markers typical of adult CMs were expressed to a greater extent in stimulated tissues compared with control cardiac constructs, however without reaching a statistical significance. Eight days of passive stimulation was relatively a short time point compared with other auxotonic studies (Leonard et al., 2018); therefore, it is possible to speculate that a longer time culture under auxotonic stimulation or the co-application of isotonic stretching could promote the switch from fetal

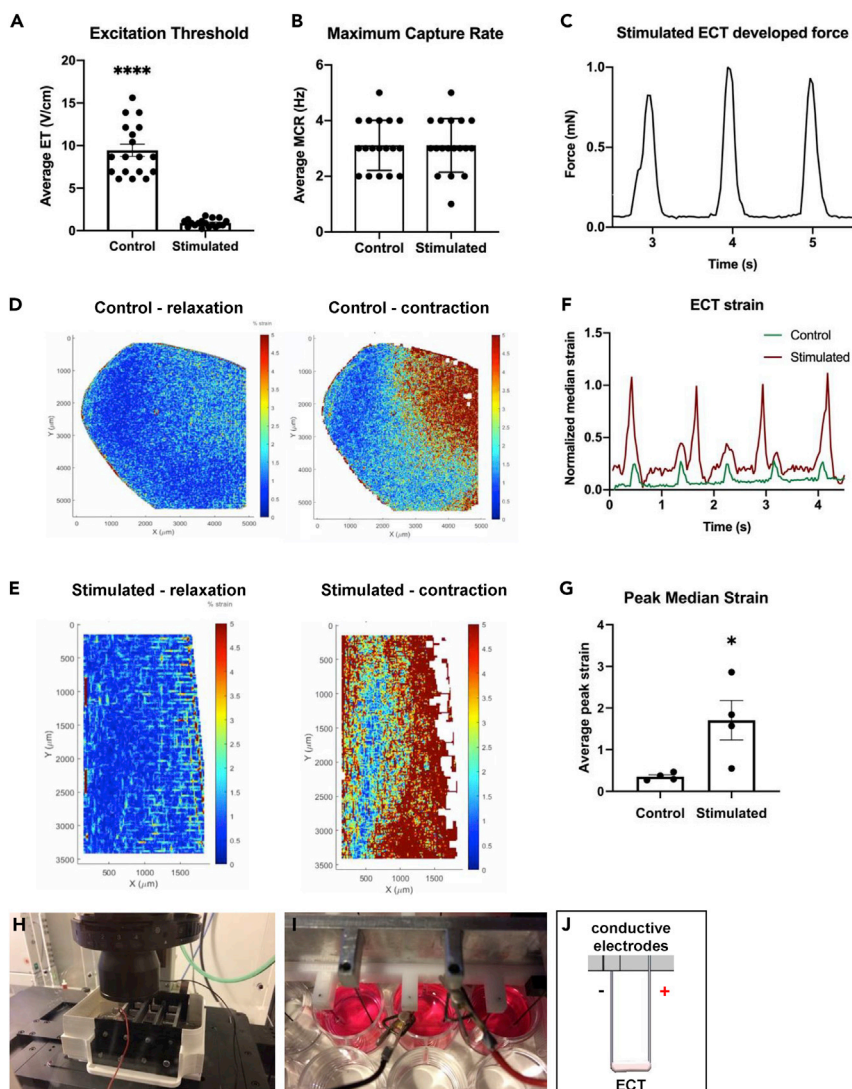


**Figure 5. ECTs electrical functionality and evaluation of force of contraction**

Graphical representation showing the normalized excitation threshold (ET, A) and the maximum capture rate (MCR, B) of control and stimulated ECTs upon electrical stimulation ( $n = 18$ , from 4 independent experiments;  $*p \leq 0.05$ ;  $****p \leq 0.0001$ ). Measured stimulated ECT force upon electrical stimulation (C). Graphical representation of beating ECT strain upon electrical stimulation (F). [Video S1](#) (Response of a statically cultured ECT to an external electrical pacing) and [Video S2](#) (Response of a ECT culture under passive stimulation to an external electrical pacing) show examples of the beating constructs analysed. Strain peak values for control ( $n = 4$ ) and stimulated ( $n = 4$ ) ECTs ( $*p \leq 0.05$ , G). [Video S3](#) (Cantilever deflection upon electrical pacing of a ECT under passive) show the cantilever deflection analyzed to evaluate the construct strain. Representative contour plot from digital image correlation (DIC) analysis of control (D) and stimulated (E) ECTs, during electrical stimulation. Electrical stimulation set-up of the bioreactor under live-imaging microscope (H). Detailed picture (I) and schematic representation (J) of the electrode set-up for one ECT replicate under live-imaging microscope. The electrical material parameters used to characterize the electrical stimulation module are summarized in [Table 1](#). Characterization of the electrical module. Data were represented as mean  $\pm$  SEM.

to adult-like phenotype. A statistically significant increase in the expression of *Myh6* to *Myh7* ratio was for instance observed by Kensah and colleagues ([Kensah et al., 2011](#)) after 7 days of ECT static culture with additional 7 days of cyclical stretch stimulation.

The contractile force measured in both neonatal and human ECTs resulted to be in the same range. Moreover, the measured contraction force was similar to the one quantified in other studies from other groups, between 0.05 and 2 mN ([Eschenhagen and Zimmermann, 2005](#); [Yang et al., 2014](#)) and almost in the same



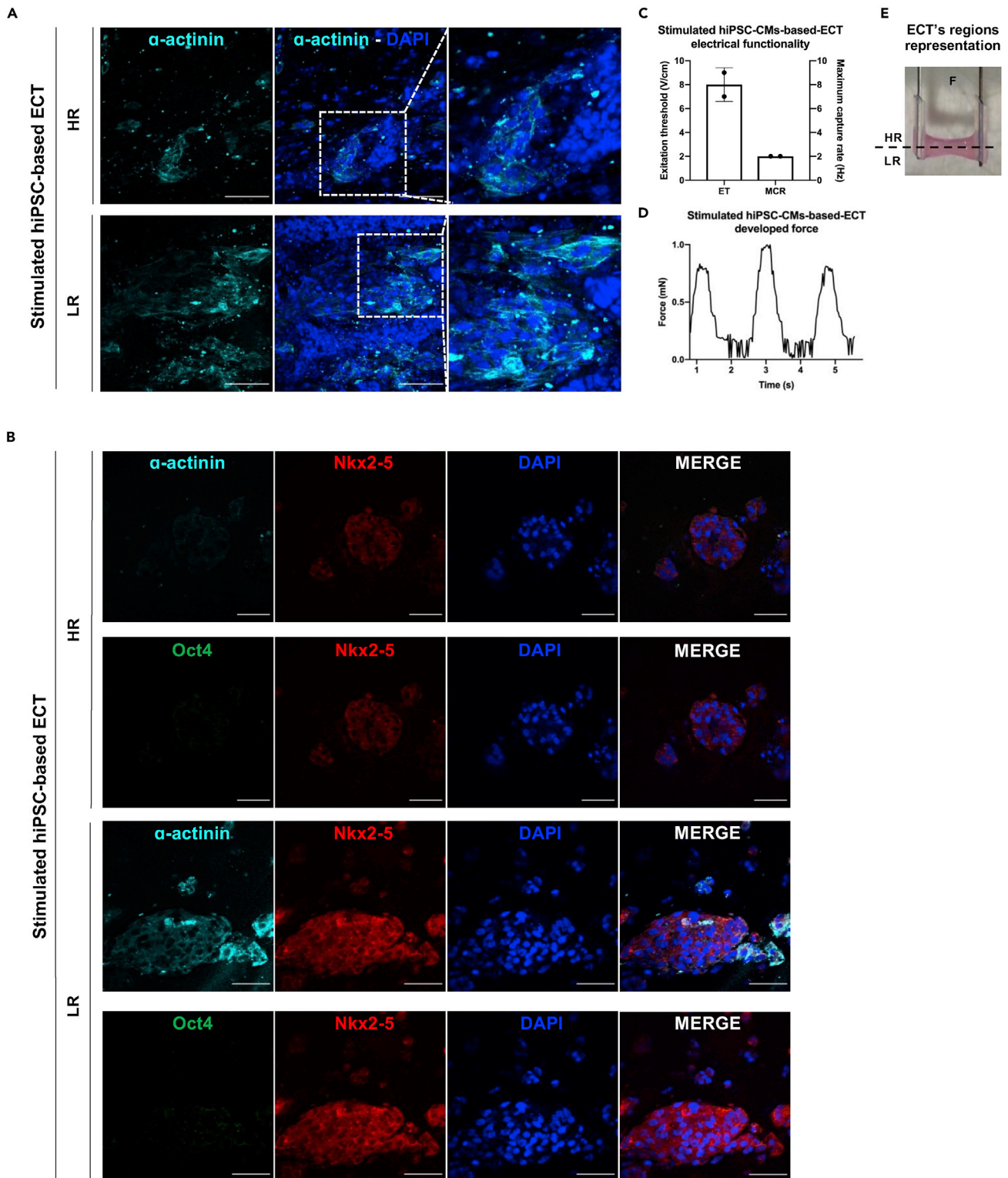




**Figure 6. Continued**

(B) Representative immunofluorescence images of stimulated ECT, high-resistance (HR) and low-resistance (LR) zones, stained for sarcomeric  $\alpha$ -actinin cardiac marker ( $\alpha$ -actinin, cyan), homeobox protein Nkx2-5 (Nkx2-5, red), and octamer-binding transcription factor 4 (Oct4, green). Nuclei were stained in blue (DAPI, blue). Scale bar: 50  $\mu$ m.

(C) Graphical representation showing the normalized excitation threshold (ET) and the maximum capture rate (MCR) of stimulated ( $n = 2$ ) ECTs upon electrical stimulation.

(D) Measured stimulated ECT force upon electrical stimulation ( $n = 1$ ).

(E) Schematic representation of the two identified zones within the stimulated ECTs. All data were represented as mean  $\pm$  SEM.

scale of the force developed from intact rat papillary muscles (around 4 mN, [Eschenhagen and Zimmermann, 2005](#)).

Leonard and colleagues ([Leonard et al., 2018](#)) investigated hiPSC-CMs maturation in ECTs applying several afterload conditions, showing that the increase of auxotonic stimulation (from 0.09 to 9.2  $\mu$ N/ $\mu$ m) improved the passive force developed by hiPSC-CMs. However, they also showed hypertrophic signs with the highest afterload condition, which corresponds to the range used in our study (12 mN/mm). The fact that in our experimental set-up hypertrophic CMs were not observed could be explained by the fact that Leonard et al. co-cultured hiPSC-CMs with human bone marrow stromal cells as support cells. In addition, the culture time was longer (3 weeks versus 8 days). Ronaldson-Bouchard et al. engineered human cardiac-like muscle in a similar fashion using hiPSC-CMs and fibroblasts in a fibrin hydrogel ([Ronaldson-Bouchard et al., 2019](#)). They showed that electromechanical stimulation using their custom-made bioreactor platform improved human-ECT functionality and maturation, either with constant training or with an increasing intensity of training, compared with nonstimulated tissues. Nonetheless, human ECTs were cultured 21 days upon exposition of both electrical and mechanical stimuli.

### Limitations of the study

In this study, we evaluated the degree of maturation and electrical functionality of CMs at the early stage of their organization within the engineered cardiac constructs. Superior culture time or combination of passive and active stimulations might be essential to achieve a superior level of maturation of the ECTs. In this way, superior differences in the gene and protein expression might be achieved allowing the generated platform to be optimized for cardiotoxicity test and drug screening. The difference observed between cell maturation and tissue organization from the HR and LR zones probably resulted from a nonuniform exposition of the cells to the same mechanical load. Notably, a difference in the decimal scale in the passive load was still sufficient to generate a clear bizonal pattern reflecting unique level of cardiac maturation. Either the extension of the time in culture or the application of isotonic cyclic stimulation might reduce this effect. To further reduce the differences in cardiac maturation observed in HR and LR regions when applying passive auxotonic stimulation, the ECT height of 4 mm could be minimized by further reducing the flexible post bending moment difference experienced at the different heights of the construct. Nevertheless, the mentioned bizonal effect might be also very useful to study heart development stages using progenitor cells and to investigate the role of passive force in this very complex process. Additional controls, such as isometric stimulation and flexible load with altered stiffness, could be considered in order to deeply study the ECT maturation. Furthermore, we focused our analysis on tissues of rat origin and only implemented a proof of concept using hiPSC-derived cardiac progenitor cells and hiPSC-derived CMs.

### Conclusion

In this study, we described a unique platform to generate and in real-time monitor miniaturized 3D engineered cardiac tissues in a reproducible and medium- to high-throughput set-up, which includes multi-physical stimuli during the culture. Development of functional ECTs based on auxotonic elastic load led to an improved contractility as well as tissue maturation and organization in terms of cardiac cell alignment in rat- and human-origin heart tissues, compared with statically cultured constructs, after only 8 days of passive stimulation. Passive stimulation generated bizonal ECTs characterized by different levels of cardiac maturation. This feature can be very useful for studying the role of mechanical forces in cardiac maturation, possibly mimicking the heart development. Future studies will include the combination of auxotonic and isotonic stimulations to further improve tissue maturation and organization. Hence, after auxotonic stimulation, the constructs can be directly and dynamically stimulated, training them to enhance their maturation phenotype. The newly designed bioreactor, thanks to the compatibility with 24-well plates and modularity and microscope-integrability features, holds great promise to investigate *in vitro* models of the heart for drug testing and for the development of patient-specific treatments but also could be easily adapted

and exploited for mechanical stimulation of other functional human organs such as skeletal muscle tissues and tendon tissues. Nevertheless, the future applications will be dedicated to the investigation of maturation of human-origin tissues driven by sequential application of different mechanical loading as well as electrical cues.

## STAR★METHODS

Detailed methods are provided in the online version of this paper and include the following:

- KEY RESOURCES TABLE
- RESOURCE AVAILABILITY
  - Lead contact
  - Materials availability
  - Data and code availability
- EXPERIMENTAL MODEL AND SUBJECT DETAILS
  - Animals
  - Cell sources
- METHOD DETAILS
  - Bioreactor design and characterization
  - Bioreactor characterization
  - Bioreactor culture
  - ECT assessments
- QUANTIFICATION AND STATISTICAL ANALYSIS

## SUPPLEMENTAL INFORMATION

Supplemental information can be found online at <https://doi.org/10.1016/j.isci.2022.104297>.

## ACKNOWLEDGMENTS

The authors would like to thank Conradin Döbeli and Giuseppe Pisani for the scientific discussion for the bioreactor development; Cinzia Tiberi from the BioEM Lab (Biozentrum, University of Basel, Basel, Switzerland) for the sample preparation, image acquisition, and data interpretation for the transmission electron microscopy analysis; Diego Calabrese (Department of Biomedicine, University of Basel, Basel, Switzerland) for iPSC expansion; as well as Katia Siciliano and Stefano Gabetti (Politecnico di Torino, Turin, Italy) for the development of the custom-made software used for DIC analysis and for the computational modeling. This study was financially supported by the Swiss National Science Foundation (310030\_172989 to A.M.).

## AUTHOR CONTRIBUTIONS

A.P., G.I., and A.M. conceived the study. G.I., G.R., and A.P. designed the bioreactor. A.P., G.I., A.S., G.P., and D.M. conducted the bioreactor modules' characterization. A.P., G.I., and A.M. designed the biological experiments. A.P., D.F., A.S., and D.R. performed the biological experiment and assessments. A.P., D.F., A.S., D.R., and H.T. analyzed the biological data. A.P. prepared the figures. G.R. and D.M. contributed to the writing of the manuscript. A.P., G.R., and A.M. reviewed the state of art. A.P., G.I., and A.M. wrote the manuscript with input and contribution from all the authors.

## DECLARATION OF INTERESTS

The authors declare no competing interests.

For full transparency policy, the authors A.P., A.M., and G.I. declare to hold a patent (number: EP19165964) covering the design of the presented bioreactor. Updated list of the current institutional affiliations of some of the authors:

- Alessia Pisanu, Nobel Biocare, Zürich-Flughafen, Switzerland
- Diana Robles Diaz, Novartis International, AG, Basel, Switzerland
- Hadi Tarhini, Northvolt, Västerås, Sweden
- Giuseppe Isu, Medics3D, Torino, Italy

Received: April 19, 2021  
Revised: November 26, 2021  
Accepted: April 21, 2022  
Published: May 20, 2022

## REFERENCES

- Bildyug, N. (2019). Extracellular matrix in regulation of contractile system in cardiomyocytes. *Int. J. Mol. Sci.* 20, 5054. <https://doi.org/10.3390/ijms20205054>.
- Boudou, T., Legant, W.R., Mu, A., Borochin, M.A., Thavandiran, N., Radisic, M., Zandstra, P.W., Epstein, J.A., Margulies, K.B., and Chen, C.S. (2012). A microfabricated platform to measure and manipulate the mechanics of engineered cardiac microtissues. *Tissue Eng. Part A* 18, 910–919. <https://doi.org/10.1089/ten.tea.2011.0341>.
- Cholewinski, E., Dietrich, M., Flanagan, T.C., Schmitz-Rode, T., and Jockenhoefel, S. (2009). Tranexamic acid—an alternative to aprotinin in fibrin-based cardiovascular tissue engineering. *Tissue Eng. Part A* 15, 3645–3653. <https://doi.org/10.1089/ten.tea.2009.0235>.
- Costa, J., Ghilardi, M., Mamone, V., Ferrari, V., Busfield, J.J.C., Ahluwalia, A., and Carpi, F. (2020). Bioreactor with electrically deformable curved membranes for mechanical stimulation of cell cultures. *Front. Bioeng. Biotechnol.* 8, 1–9. <https://doi.org/10.3389/fbioe.2020.00022>.
- Dostanic, M., Windt, L., Stein, J., van Meer, B., Mastrangeli, M., Mummery, C., and Sarro, L. (2019). A miniaturized EHT platform for contractile tissue measurements. In *International MicroNanoConference*.
- Eschenhagen, T., Fink, C., Remmers, U., Scholz, H., Wattchow, J., Weil, J., Zimmermann, W., Dohmen, H.H., Schafer, H., Bishopric, N., et al. (1997). Three-dimensional reconstitution of embryonic cardiomyocytes in a collagen matrix: a new heart muscle model system. *FASEB J.* 11, 683–694. <https://doi.org/10.1096/fasebj.11.8.9240969>.
- Eschenhagen, T., and Zimmermann, W.H. (2005). Engineering myocardial tissue. *Circ. Res.* 97, 1220–1231. <https://doi.org/10.1161/01.RES.0000196562.73231.7d>.
- Goldfracht, I., Efraim, Y., Shinnawi, R., Kovalev, E., Huber, I., Gepstein, A., Arbel, G., Shaheen, N., Tiburcy, M., Zimmermann, W.H., et al. (2019). Engineered heart tissue models from hiPSC-derived cardiomyocytes and cardiac ECM for disease modeling and drug testing applications. *Acta Biomater.* 92, 145–159. <https://doi.org/10.1016/j.actbio.2019.05.016>.
- Griffith, L.G., and Swartz, M.A. (2006). Capturing complex 3D tissue physiology *in vitro*. *Nat. Rev. Mol. Cell Biol.* 7, 211–224. <https://doi.org/10.1038/nrm1858>.
- Hinson, J.T., Chopra, A., Nafissi, N., Polacheck, W.J., Benson, C.C., Swift, S., Gorham, J., Yang, L., Schafer, S., Sheng, C.C., et al. (2015). Titin mutations in iPS cells define sarcomere insufficiency as a cause of dilated cardiomyopathy. *Science* 349, 982–986. <https://doi.org/10.1126/science.aaa5458>.
- Hirt, M.N., Hansen, A., and Eschenhagen, T. (2014). Cardiac tissue engineering : state of the art. *Circ. Res.* 114, 354–367. <https://doi.org/10.1161/CIRCRESAHA.114.300522>.
- Hogenes, A.M., Slump, C.H., te Riet o.g. Scholten, G.A., Meijerink, M.R., Futterer, J.J., van Laarhoven, C.J.H.M., Overduin, C.G., and Stommel, M.W.J. (2020). Effect of irreversible electroporation parameters and the presence of a metal stent on the electric field line pattern. *Sci. Rep.* 10, 13517–13612. <https://doi.org/10.1038/s41598-020-70308-3>.
- Hom, J.R., Quintanilla, R., Hoffman, D., de Mesy Bentley, K., Molkentin, J., Sheu, S.S., and Porter, G. (2011). The permeability transition pore controls cardiac mitochondrial maturation and myocyte differentiation. *Dev. Cell* 21, 469–478. <https://doi.org/10.1016/j.devcel.2011.08.008>.
- Jiang, Y., Park, P., Hong, S.M., and Ban, K. (2018). Maturation of cardiomyocytes derived from human pluripotent stem cells: current strategies and limitations. *Mol. Cells* 41, 613–621. <https://doi.org/10.14348/molcells.2018.0143>.
- Karbassi, E., Fenix, A., Marchiano, S., Muraoka, N., Nakamura, K., Yang, X., and Murry, C.E. (2020). Cardiomyocyte maturation: advances in knowledge and implications for regenerative medicine. *Nat. Rev. Cardiol.* 17, 341–359. <https://doi.org/10.1038/s41569-019-0331-x>.
- Kempf, H., Kropp, C., Olmer, R., Martin, U., and Zweigerdt, R. (2015). Cardiac differentiation of human pluripotent stem cells in scalable suspension culture. *Nat. Protoc.* 10, 1345–1361. <https://doi.org/10.1038/nprot.2015.089>.
- Kempf, H., Olmer, R., Haase, A., Franke, A., Bolesani, E., Schwanke, K., Robles-Diaz, D., Coffee, M., Gohring, G., Drager, G., et al. (2016). Bulk cell density and Wnt/TGFbeta signalling regulate mesodermal patterning of human pluripotent stem cells. *Nat. Commun.* 7, 13602. <https://doi.org/10.1038/ncomms13602>.
- Kensah, G., Gruh, I., Viering, J., Schumann, H., Dahlmann, J., Meyer, H., Skvorc, D., Bar, A., Akhyari, P., Heisterkamp, A., et al. (2011). A novel miniaturized multimodal bioreactor for continuous in situ assessment of bioartificial cardiac tissue during stimulation and maturation. *Tissue Eng. Part C Methods* 17, 463–473. <https://doi.org/10.1089/ten.tec.2010.0405>.
- Kostetskii, I., Li, J., Xiong, Y., Zhou, R., Ferrari, V.A., Patel, V.V., Molkentin, J.D., and Radice, G.L. (2005). Induced deletion of the N-cadherin gene in the heart leads to dissolution of the intercalated disc structure. *Circ. Res.* 96, 346–354. <https://doi.org/10.1161/01.RES.0000156274.72390.2c>.
- Leonard, A., Bertero, A., Powers, J.D., Beussman, K.M., Bhandari, S., Regnier, M., Murry, C.E., and Sniadecki, N.J. (2018). Afterload promotes maturation of human induced pluripotent stem cell derived cardiomyocytes in engineered heart tissues. *J. Mol. Cell Cardiol.* 118, 147–158. <https://doi.org/10.1016/j.jmcc.2018.03.016>.
- Lian, X., Zhang, J., Azarin, S.M., Zhu, K., Hazeltine, L.B., Bao, X., Hsiao, C., Kamp, T.J., and Palecek, S.P. (2013). Directed cardiomyocyte differentiation from human pluripotent stem cells by modulating Wnt/ $\beta$ -catenin signaling under fully defined conditions. *Nat. Protoc.* 8, 162–175. <https://doi.org/10.1038/nprot.2012.150>.
- Liaw, N.Y., and Zimmermann, W.H. (2016). Mechanical stimulation in the engineering of heart muscle. *Adv. Drug Deliv. Rev.* 96, 156–160. <https://doi.org/10.1016/j.addr.2015.09.001>.
- Lu, H.R., Whittaker, R., Price, J.H., Vega, R., Pfeiffer, E.R., Cerignoli, F., Towart, R., and Gallacher, D.J. (2015). High throughput measurement of Ca<sup>++</sup> dynamics in human stem cell-derived cardiomyocytes by kinetic image cytometry: a cardiac risk assessment characterization using a large panel of cardioactive and inactive compounds. *Toxicol. Sci.* 148, 503–516. <https://doi.org/10.1093/toxsci/kfv201>.
- Lux, M., Andree, B., Horvath, T., Nosko, A., Manikowski, D., Hilfiker-Kleiner, D., Haverich, A., and Hilfiker, A. (2016). In vitro maturation of large-scale cardiac patches based on a perfusable starter matrix by cyclic mechanical stimulation. *Acta Biomater.* 30, 177–187. <https://doi.org/10.1016/j.actbio.2015.11.006>.
- Marsano, A., Conficconi, C., Lemme, M., Occhetta, P., Gaudiello, E., Votta, E., Cerino, G., Redaelli, A., and Rasponi, M. (2016). Beating heart on a chip: a novel microfluidic platform to generate functional 3D cardiac microtissues. *Lab Chip* 16, 599–610. <https://doi.org/10.1039/c5lc01356a>.
- Massai, D., Cerino, G., Gallo, D., Pennella, F., Deriu, M., Rodriguez, A., Montevicchi, F., Bignardi, C., Audenino, A., and Morbiducci, U. (2013). Bioreactors as engineering support to treat cardiac muscle and vascular disease. *J. Healthc. Eng.* 4, 329–370. <https://doi.org/10.1260/2040-2295.4.3.329>.
- Massai, D., Pisani, G., Isu, G., Rodriguez Ruiz, A., Cerino, G., Galluzzi, R., Pisanu, A., Tonoli, A., Bignardi, C., Audenino, A.L., et al. (2020). Bioreactor platform for biomimetic culture and in situ monitoring of the mechanical response of *in vitro* engineered models of cardiac tissue. *Front. Bioeng. Biotechnol.* 8, 1–14. <https://doi.org/10.3389/fbioe.2020.00733>.
- Mittal, R., Woo, F.W., Castro, C.S., Cohen, M.A., Karanxha, J., Mittal, J., Chhibber, T., and Jhaveri, V.M. (2019). Organ-on-chip models: implications in drug discovery and clinical applications. *J. Cell Physiol.* 234, 8352–8380. <https://doi.org/10.1002/jcp.27729>.

- Morgan, K.Y., and Black, L.D. (2014). Mimicking isovolumic contraction with combined electromechanical stimulation improves the development of engineered cardiac constructs. *Tissue Eng. Part A* 20, 1654–1667. <https://doi.org/10.1089/ten.tea.2013.0355>.
- Nugraha, B., Buono, M.F., Boehmer, L., Hoerstrup, S.P., and Emmert, M.Y. (2019). Human cardiac organoids for disease modeling. *Clin. Pharmacol. Ther.* 105, 79–85. <https://doi.org/10.1002/cpt.1286>.
- Oliver-Gelabert, A., Garcia-Mendivil, L., Vallejo-Gil, J.M., Fresneda-Roldan, P.C., Andelova, K., Fananas-Mastral, J., Vazquez-Sancho, M., Matamala-Adell, M., Sorribas-Berjon, F., Ballester-Cuenca, C., et al. (2020). Automatic quantification of cardiomyocyte dimensions and connexin 43 lateralization in fluorescence images. *Biomolecules* 10, 1334–1425. <https://doi.org/10.3390/biom10091334>.
- Pavesi, A., Soncini, M., Zamperone, A., Pietronave, S., Medico, E., Redaelli, A., Prat, M., and Fiore, G.B. (2014). Electrical conditioning of adipose-derived stem cells in a multi-chamber culture platform. *Biotechnol. Bioeng.* 111, 1452–1463. <https://doi.org/10.1002/bit.25201>.
- Putame, G., Gabetti, S., Carbonaro, D., Meglio, F.D., Romano, V., Sacco, A.M., Belviso, I., Serino, G., Bignardi, C., Morbiducci, U., et al. (2020). Compact and tunable stretch bioreactor advancing tissue engineering implementation. Application to engineered cardiac constructs. *Med. Eng. Phys.* 84, 1–9. <https://doi.org/10.1016/j.medengphy.2020.07.018>.
- Qi, X.Y., Yan, D., Jiang, Z., Cao, Y.K., Yu, Z.Z., Yavari, F., and Koratkar, N. (2011). Enhanced electrical conductivity in polystyrene nanocomposites at ultra-low graphene content. *ACS Appl. Mater. Interfaces* 3, 3130–3133. <https://doi.org/10.1021/am200628c>.
- Radisic, M., Marsano, A., Maidhof, R., Wang, Y., and Vunjak-Novakovic, G. (2008). Cardiac tissue engineering using perfusion bioreactor systems. *Nat. Protoc.* 3, 719–738. <https://doi.org/10.1038/nprot.2008.40>.
- Ribeiro, A.J.S., Guth, B.D., Engwall, M., Eldridge, S., Foley, C.M., Guo, L., Gintant, G., Koerner, J., Parish, S.T., Pierson, J.B., et al. (2019). Considerations for an *in vitro*, cell-based testing platform for detection of drug-induced inotropic effects in early drug development. Part 2: designing and fabricating microsystems for assaying cardiac contractility with physiological relevance using human iPSC-cardiomyocytes. *Front. Pharmacol.* 10, 1–19. <https://doi.org/10.3389/fphar.2019.00934>.
- Ronaldson-Bouchard, K., Ma, S.P., Yeager, K., Chen, T., Song, L., Sirabella, D., Morikawa, K., Teles, D., Yazawa, M., and Vunjak-Novakovic, G. (2018). Advanced maturation of human cardiac tissue grown from pluripotent stem cells. *Nature* 556, 239–243. <https://doi.org/10.1038/s41586-018-0016-3>.
- Ronaldson-Bouchard, K., Yeager, K., Teles, D., Chen, T., Ma, S., Song, L., Morikawa, K., Wobma, H.M., Vasciaveo, A., Ruiz, E.C., et al. (2019). Engineering of human cardiac muscle electromechanically matured to an adult-like phenotype. *Nat. Protoc.* 14, 2781–2817. <https://doi.org/10.1038/s41596-019-0189-8>.
- Sbalzarini, I.F., and Koumoutsakos, P. (2005). Feature point tracking and trajectory analysis for video imaging in cell biology. *J. Struct. Biol.* 151, 182–195. <https://doi.org/10.1016/j.jsb.2005.06.002>.
- Stoppel, W.L., Kaplan, D.L., and Black, L.D. (2016). Electrical and mechanical stimulation of cardiac cells and tissue constructs. *Adv. Drug Deliv. Rev.* 96, 135–155. <https://doi.org/10.1016/j.addr.2015.07.009>.
- Tandon, N., Cannizzaro, C., Chao, P.H.G., Maidhof, R., Marsano, A., Au, H.T.H., Radisic, M., and Vunjak-Novakovic, G. (2009). Electrical stimulation systems for cardiac tissue engineering. *Nat. Protoc.* 4, 155–173. <https://doi.org/10.1038/nprot.2008.183>.
- Thavandiran, N., Hale, C., Blit, P., Sandberg, M.L., McElvain, M.E., Gagliardi, M., Sun, B., Witty, A., Graham, G., Do, V., et al. (2020). Functional arrays of human pluripotent stem cell-derived cardiac microtissues. *Sci. Rep.* 10, 6919–7013. <https://doi.org/10.1038/s41598-020-62955-3>.
- Tsai, P.J., Nayak, S., Ghosh, S., and Puri, I.K. (2017). Influence of particle arrangement on the permittivity of an elastomeric composite. *AIP Adv.* 7, 015003–015008. <https://doi.org/10.1063/1.4973724>.
- Veldhuizen, J., Migrino, R.Q., and Nikkiah, M. (2019). Three-dimensional microengineered models of human cardiac diseases. *J. Biol. Eng.* 13, 29. <https://doi.org/10.1186/s13036-019-0155-6>.
- Veldhuizen, J., Cutts, J., Brafman, D.A., Migrino, R.Q., and Nikkiah, M. (2020). Engineering anisotropic human stem cell-derived three-dimensional cardiac tissue on-a-chip. *Biomaterials* 256, 120195. <https://doi.org/10.1016/j.biomaterials.2020.120195>.
- Visone, R., Gilardi, M., Marsano, A., Rasponi, M., Bersini, S., and Moretti, M. (2016). Cardiac meets skeletal: what's new in microfluidic models for muscle tissue engineering. *Molecules* 21, 1128–1221. <https://doi.org/10.3390/molecules21091128>.
- Vite, A., and Radice, G.L. (2014). N-cadherin/catenin complex as a master regulator of intercalated disc function. *Cell Commun. Adhes.* 21, 169–179. <https://doi.org/10.3109/15419061.2014.908853>.
- Wright, P.T., Tsui, S.F., Francis, A.J., MacLeod, K.T., and Marston, S.B. (2020). Approaches to high-throughput analysis of cardiomyocyte contractility. *Front. Physiol.* 11, 1–19. <https://doi.org/10.3389/fphys.2020.00612>.
- Yang, X., Pabon, L., and Murry, C.E. (2014). Engineering adolescence: Maturation of human pluripotent stem cell-derived cardiomyocytes. *Circ. Res.* 114, 511–523. <https://doi.org/10.1161/CIRCRESAHA.114.300558>.
- Ye Morgan, K., and Black, L.D. (2014). It's all in the timing Modeling isovolumic contraction through development and disease with a dynamic dual electromechanical bioreactor system. *Organogenesis* 10, 317–322. <https://doi.org/10.4161/org.29207>.
- Yuxuan, G., and Pu, W.T. (2020). Cardiomyocyte maturation. *Circ. Res.* 126, 1086–1106. <https://doi.org/10.1161/CIRCRESAHA.119.315862>.
- Zhao, Q., Sun, Q., Zhou, L., Liu, K., and Jiao, K. (2019a). Complex regulation of mitochondrial function during cardiac development. *J. Am. Heart Assoc.* 8, 1–12. <https://doi.org/10.1161/JAHA.119.012731>.
- Zhao, Y., Rafatian, N., Feric, N.T., Cox, B.J., Aschar-Sobbi, R., Wang, E.Y., Aggarwal, P., Zhang, B., Conant, G., Ronaldson-Bouchard, K., et al. (2019b). A platform for generation of chamber-specific cardiac tissues and disease modeling. *Cell* 176, 913–927.e18. <https://doi.org/10.1016/j.cell.2018.11.042>.
- Zimmermann, J., Distler, T., Boccaccini, A.R., and van Rienen, U. (2020). Numerical simulations as means for tailoring electrically conductive hydrogels towards cartilage tissue engineering by electrical stimulation. *Molecules* 25, 4750–4821. <https://doi.org/10.3390/molecules25204750>.
- Zimmermann, W.H., Schneiderbanger, K., Schubert, P., Didié, M., Münzel, F., Heubach, J., Kostin, S., Neuhuber, W., and Eschenhagen, T. (2002). Tissue engineering of a differentiated cardiac muscle construct. *Circ. Res.* 90, 223–230. <https://doi.org/10.1161/hh0202.103644>.
- Zuppinger, C. (2019). 3D cardiac cell culture: a critical review of current Technologies and applications. *Front. Cardiovasc. Med.* 6, 1–9. <https://doi.org/10.3389/fcvm.2019.00087>.

## STAR★METHODS

### KEY RESOURCES TABLE

REAGENT or RESOURCE	SOURCE	IDENTIFIER
<b>Antibodies</b>		
anti-cardiac Troponin-T	Myltenyi Biotec	RRID: 130-120-543
mouse monoclonal anti-sarcomeric $\alpha$ -actinin	Abcam	ABCAM9465; RRID:AB_307264
Alexa488 F-actin	Invitrogen, Thermo Fisher Scientific	RRID: A-12379
mouse monoclonal IgG2a $\alpha$ -SMA	Sigma-Aldrich	A-2547; RRID:AB_476701
rabbit polyclonal IgG Ki67	Abcam	15580; RRID:AB_443209
Alexa 647 anti-mouse	Life Technologies, Thermo Fisher Scientific	A-21240; RRID:AB_2535809
Alexa 546 anti-mouse	Life Technologies, Thermo Fisher Scientific	A-21133; RRID:AB_2535772
Alexa 546 anti-rabbit	Life Technologies, Thermo Fisher Scientific	A-11035; RRID:AB_2534093
Alexa 488 anti-mouse	Life Technologies, Thermo Fisher Scientific	A-21141; RRID:AB_2535778
Alexa 546 anti-mouse	Life Technologies, Thermo Fisher Scientific	A-21123; RRID:AB_2535765
<b>Chemicals, peptides, and recombinant proteins</b>		
EDTA-free tablet	Roche	11873580001
TGX gels	Bio-Rad	4561085
Trans-Blot Turbo Transfer System	Bio-Rad	1704156
Chemiluminescent substrate	Thermo Fisher Scientific	32209
Hepes	Sigma-Aldrich	H0887
Penicillin/Streptomycin	Sigma-Aldrich	P4333
L-glutamine	Sigma-Aldrich	G7513
Rho kinase inhibitor Y-27632	Calbiochem	688000
CHIR99021 molecule	MilliporeSigma	cat. no. 361571
tranexamic-acid	Sigma-Aldrich	857653
paraformaldehyde (PFA)	Sigma-Aldrich	15710
Glutaraldehyde	Electron Microscopy Sciences	16310
Osmium tetroxide	Electron Microscopy Sciences	19100
Uranyl acetate	Electron Microscopy Sciences	22400
Acetone	Electron Microscopy Sciences	15056
Epon812 resin	Electron Microscopy Sciences	14120
Trypsin from bovine pancreas	Sigma-Aldrich	T9201
Collagenase type 2	Worthington-Biochem	LS004176
Fibrinogen	Sigma-Aldrich	F3879
Thrombin	Sigma-Aldrich	T6884
Eosin 1%	Biosystems	84-0012-00
Harris's haematoxylin	Biosystems	3873.1000
4',6-diamidino-2-phenylindole (DAPI)	Sigma-Aldrich	32670
<b>Critical commercial assays</b>		
FIX&PERM cell fixation and permeabilization kit	Invitrogen, Thermo-Fisher Scientific	GAS003
Sylgard 184 Silicone Elastomer Kit	Ellsworth Adhesives	01673921
Superscript III REV transcript 10,000 UN kit	Thermo-Fisher Scientific	18080044
TaqMan assays master mix	Thermo-Fisher Scientific	4369016
Pierce BCA Protein Assay Kit	Thermo Fisher Scientific	23225
LIVE-DEAD staining	Invitrogen, Thermo-Fisher Scientific	L3224

(Continued on next page)



### Continued

REAGENT or RESOURCE	SOURCE	IDENTIFIER
Experimental models: Cell lines		
Human: iPSC	ATCC	ACS-1011
Oligonucleotides		
Connexin 43 <i>Gaj1</i>	Thermo-Fisher Scientific	Rn01433957_m1
Troponin I <i>Tnni3</i>	Thermo-Fisher Scientific	Rn00437164_m1
Myosin light chain2 ventricular <i>Myl2</i>	Thermo-Fisher Scientific	Rn02769676_s1
Myosin light chain7 atrial <i>Myl7</i>	Thermo-Fisher Scientific	Rn01752521_g1
Myosin heavy chain 7 <i>Myh7</i>	Thermo-Fisher Scientific	Rn01488777_g1
Myosin heavy chain 6 <i>Myh6</i>	Thermo-Fisher Scientific	Rn00691721_g1
N-Cadherin <i>Cdh2</i>	Thermo-Fisher Scientific	Rn00580099_m1
Tenascin C <i>Tnc</i>	Thermo-Fisher Scientific	Rn01454947_m1
Collagen type I <i>Col1a1</i>	Thermo-Fisher Scientific	Rn01463848_m1
Collagen type III <i>Col3a</i>	Thermo-Fisher Scientific	Rn01437681_m1
$\alpha$ -smooth muscle actin <i>Acta2</i>	Thermo-Fisher Scientific	Rn01759928_g1
Matrix Metalloproteinase 9 <i>Mmp9</i>	Thermo-Fisher Scientific	Rn00579162_m1
Glyceraldehyde-3-phosphate dehydrogenase <i>Gapdh</i>	Thermo-Fisher Scientific	Rn01775763_g1
Software and algorithms		
Digital Image Correlation (DIC)	MATLAB	N/A
ParticleTracker ImageJ/Fiji Plugin MOSAICO	ImageJ/Fiji	N/A
Other		
High Glucose Dulbecco Modified Eagle's Medium	Sigma-Aldrich	D5671
fetal bovine serum	Sigma-Aldrich	F9665
Geltrex basement membrane matrix	Invitrogen, Thermo Fisher Scientific	A1413202
mTESR1	STEMCELL Technologies	85850
B27 supplement without insulin	Life Technology	A18956-01
RPMI 1640	Life Technology	21875-034
IWP2	Tocris Bioscience	3533
B27 supplement with insulin	Life Technology	17504-044
PIPES buffer	Sigma-Aldrich	P6757
Phosphate-buffered saline (PBS)	Sigma-Aldrich	D8537

## RESOURCE AVAILABILITY

### Lead contact

Further information and requests for resources and reagents should be directed to and will be fulfilled by the lead contact Anna Marsano ([anna.marsano@usb.ch](mailto:anna.marsano@usb.ch)).

### Materials availability

This study did not generate nor use any new or unique reagents.

### Data and code availability

- All data produced in this study are included in the published article and its [supplemental information](#), or are available from the [lead contact](#) upon request.
- This paper does not report original code.

- Any additional information required to reanalyze the data reported in this paper is available from the [lead contact](#) upon request.

## EXPERIMENTAL MODEL AND SUBJECT DETAILS

### Animals

All animal experiments involving animal care, surgery, and sample preparation were approved by the Cantonal Veterinary Office in Basel, Switzerland (Approval No. 2608\_30631) and conducted in accordance with Fundamental Guidelines for Proper Conduct of Animal Experiments by the Swiss Federal Food Safety and Veterinary Office and the Federation of European Laboratory Animal Science Association. All efforts were made to minimize animal suffering and the number of animals used. Under this license, 2–3-days old neonatal pups were sacrificed by decapitation and the hearts collected and digested to isolate the cells. The sex of the pups was unknown.

### Cell sources

#### *Neonatal rat cardiomyocytes isolation*

Neonatal rat cardiomyocytes (NRCMs) were isolated from 2–3-days old Sprague Dawley rats (Radisic et al., 2008). Briefly, rat ventricles were minced in small pieces and digested overnight in 0.06% w/v trypsin solution (trypsin from bovine pancreas, Sigma-Aldrich, USA) under continuous shaking at 50–60 oscillation per min at 4°C. The digestion of the minced tissues was continued by five consecutive 4-min cycles of 0.1% w/v collagenase solution treatment (collagenase type 2, Worthington-Biochem, USA). Isolated cardiac cells were then pre-plated in culture flasks for 45 min at 37°C and at 5% CO<sub>2</sub> to allow fibroblast adhesion and enrich the cell population for NRCMs. The enriched cardiac population was seeded a density of  $6 \times 10^4$  cells/cm<sup>2</sup> and cultured with high glucose Dulbecco Modified Eagle's Medium (DMEM, Sigma-Aldrich, USA), supplemented with 1% HEPES (Sigma-Aldrich, USA), 1% Penicillin/Streptomycin (Sigma-Aldrich, USA), 1% L-glutamine (Sigma-Aldrich, USA) and 10% fetal bovine serum (FBS, Sigma-Aldrich, USA) (standard medium) for 24 h before starting the experiments.

#### *Human induced pluripotent stem cell-derived cardiomyocytes (hiPSC-CMs)*

Human induced pluripotent stem cells (hiPSCs) were differentiated into functional cardiomyocytes (CMs) by using the chemical WNT pathway modulator CHIR99021 (Lian et al., 2013; Kempf et al., 2015, 2016). hiPSCs (ATCC® ACS1011™) were seeded in Geltrex (GT)-coated (Geltrex basement membrane matrix, Invitrogen, Thermo Fisher Scientific, USA) (day -4) at a low passage in a 12-well plate with a total cell density of  $1.5 \times 10^5$  cells per well in the fully defined media mTESR1 (cat. no. 85850, STEMCELL Technologies, Canada) supplemented with Rho kinase inhibitor Y-27632 (Calbiochem, USA). After 4 days of cell expansion (day 0), 10 μM CHIR99021 molecule (MilliporeSigma, USA, cat. no. 361571) was added in RB<sup>−</sup> medium, composed by B27 supplement without insulin (cat. no. A18956-01, Life Technology, USA) and RPMI 1640 (cat. no. 21875-034, Life Technology, Gibco, USA) with 1:50 dilution. Media change was performed after 24 h using RB<sup>−</sup> medium. At day 3, media change (RB<sup>−</sup> medium) was supplemented with 5 μM IWP2 (cat. no. 3533, Tocris Bioscience, United Kingdom). At day 5, IWP2 inhibitor was removed and added RB<sup>−</sup> medium. After 48 h (day 7), media change was made using RB<sup>+</sup> medium, including B27 supplement with insulin (cat. no. 17504-044, Life Technology, USA) and RPMI 1640, with 1:50 dilution. On day 9, fresh RB<sup>+</sup> medium was added and at day 10 cells were analyzed with flow cytometric analysis (Cytoflex, Beckman Coulter, USA). Cells were stained with LIVE-DEAD staining (Invitrogen, Thermo-Fisher Scientific, USA), to discern between living and dead cells, fixed and permeabilized with FIX&PERM cell fixation and permeabilization kit (Invitrogen, Thermo-Fisher Scientific, USA) and with fluorescent dye-tagged antibody anti-cardiac Troponin-T (Mytenyi Biotec, Germany), for CMs content quantification.

## METHOD DETAILS

### Bioreactor design and characterization

#### *Bioreactor description*

A mm-scale microscope-integrable bioreactor was designed in order to apply multiple mechanical and electrical stimuli to the cultured ECTs, mimicking the physiological and pathological conditions present in the native heart (patent number: EP19165964). The bioreactor was conceived as a modular structure to be fully incorporated with standard laboratory equipment, such as 24-well culture plates, and to be image-compatible by the integration with standard microscopy systems for live imaging. The bioreactor

consisted of a 3D printed frame (Figure 1A-c.), made of polylactide acid (PLA) (MakerBot Replicator<sup>+</sup> printer, USA), and the mechanical stimulation module (Figure 1A-b.) positioned in a conventional 24-well culture plate (Figure 1A-d.). The mechanical stimulation module was composed of six submodules, one for each of the columns of the plate (Figure S1A), which allowed independent mechanical stimulation to one column composed of four separated and independent culture wells (Figure S1B). The individual sub-modules were designed in order to apply the same mechanical stimulation to four ECT replicates (one per culture well), and make each well accessible both for real-time optical investigation and sample manipulation during the culture period (Figures 1B and 1C).

### Mechanical stimulation module

Mechanical stimulation of ECTs was achieved by casting a cell-based fibrin gels between two metal wires (Figure 1D): one flexible, made of nitinol (Fort Wayne Metals, USA), a Nickel-Titanium alloy, and the other rigid made of stainless steel (Sadevinox, France). The wires were constrained in two independent, yet solid bodies: the nitinol wires were attached directly to the main bioreactor frame (blue-colored framed component in Figure S1C), while the stainless-steel wires were fixed to a comb-like structure. This latter allowed to adjust the initial ECT length by sliding with respect to the main body (green-colored framed component in Figure S1C) by stainless-steel screws. The mentioned independent bodies were kept in position by attaching them to two lateral plastic components of the main bioreactor frame (red-colored framed component in Figure S1C). Both nitinol and stainless-steel wires presented a cross-section of circular shape (diameter = 0.4 mm), and they were oriented parallel and aligned, with an adjustable distance (8–12 mm) that could be adjusted by sliding the comb-like component. The Nitinol wires were exploited to apply passive loading into the ECTs. To maximize the deformation of the nitinol wires, they were positioned at the highest frame point to obtain a cantilever length of 41.5 mm. On the contrary, to maximize the stiffness of the rigid wires, the stainless-steel wires were 27.5 mm in length. Each ECT casted between a flexible wire and a rigid one was able to contract and develop a passive force by bending the nitinol wire. The stainless-steel rigid wires can be instead used to deliver isotonic stimulation (Figure 1F). Hence, the mentioned rigid wires were fixed in a moving shaft, which can be connected with a driving motor that delivers the cyclical stretch on the tissue.

### Auxotonic stimulation and force measurement

The flexible nitinol wire was used to apply a passive loading (auxotonic stimulation) and to measure the force contraction developed by the ECT (Figure 1F). Nitinol, due to its so-called “superelastic” behavior, is capable of deforming under an applied force and consequently recovering to its original unstressed shape upon the removal of the force. Moreover, for small deformations (up to 10% deformation strain) the material stress-strain curve is maintained in the linear elastic range. The wire bending is directly proportional to the passive force produced by the ECT during the maturation and remodeling processes: the larger the force applied, the larger is the deformation of the cantilever. The contraction force  $F$  exerted by the ECT can be quantified by using the known nitinol wire stiffness  $k$  and the deflection  $d$ , the latter being optically detected by the microscope camera, using the following formula:

$$d = \frac{FL_c^3}{3EJ}$$

Where  $L_c$  is the cantilever length,  $E$  is the Nitinol Young’s modulus, and  $J$  is the moment of inertia. The ratio  $3EJ/L^3$  represents the cantilever bending stiffness  $k$ , parameter calibrated as described in paragraph 1.6.1 (Figures S2A and S2B).

### Isotonic stimulation module

For applying isotonic cyclic load to the ECTs, the bioreactor can be equipped with an actuation system driven by a captive stepper motor (NEMA 14, Nanotec Electronic GmbH & Co. KG, Feldkirchen, DE) that generates a linear motion with a resolution of 10  $\mu\text{m}/\text{step}$  (Putame et al., 2020). The stepper motor controls the cyclic translation of the mechanical stimulation module’s comb-like structure, in which the stainless steel wires are fixed. Therefore, the mentioned structure can slide respect to the main body of the mechanical stimulation module following a defined waveform, and delivering different mechanical loading protocols to the ECTs. In particular, the isotonic stimulation module can generate cyclic motions (e.g., triangular, sinusoidal) with tunable stretching amplitudes (0.1–3.0 mm, by steps of 0.1 mm) and frequencies (1–3 Hz, by steps of 0.5 Hz).

### Electrical stimulation module

The metal wires were also exploited to apply electrical stimuli directly on the ECT (Figure 1F). The wires were used as electrodes connected to a customised stimulator, which allows the application of squared waves of 2 ms of duration at different frequencies (1–4 Hz) and amplitudes (1–23 V). Customized PDMS electrical tubes were positioned as support around the metal wires for a total height of 5 mm and the wires tips were left free for 0.5 mm to avoid high voltages on the parts of the portion of the ECT constructs in contact with the electrodes.

### Bioreactor characterization

#### Auxotonic stimulation module

A quasi-static calibration process was implemented to characterize the nitinol wires as force sensors. A tensile force machine (MTS Systems Corporation, USA), controlled in displacement, was used to impose a deflection ramp to the nitinol wire with a known varying speed of 0.017 mm/s. Particularly, the wire was mounted on the moving extremity of the test machine and pushed against a metal pin located at the tip of the cantilever and with a contact area corresponding to the width of the ECTs. In this way, the calibration procedure assured the mimicking of the tensile force produced by the ECT on the wire. For each displacement applied (i.e. the maximum deflection of the bending cantilever), the force exerted by the deformed cantilever was measured with a 0–2 N load cell (MTS Synergy, MTS Systems Corporation, USA). A force vs displacement graph was calculated for a 160 s test. Force/displacement couples were linearly fitted (forcing intercept equal 0 i.e., for null displacement null force,  $R^2 = 0.993$ ) and the angular coefficient of the line represented the cantilever stiffness  $k$ , calculated equal to 12 mN/mm (Figures S2A and S2B).

The difference in deformation strain is calculated using the beam elastic curve equation:

$$w(x) = \frac{Px^2(3L - x)}{6EI}$$

Where  $w(x)$  is the deformation strain at a generic  $x$  distance from the fixed end of the cantilever. Based on the cantilever calibration data (Figures S2A and S2B), the relative strain difference between HR and LR zones is therefore calculated as

$$\frac{w(x_{HR}) - w(x_{LR})}{w(x_{HR})} 100$$

#### Isotonic stimulation module

The isotonic stimulation module was characterized using a linear variable displacement transducer (LVDT, AML/EU/±5/S, Applied Measurements Ltd., Aldermaston, UK) mounted on a chassis and connected to a data acquisition system (Personal computer equipped with a cDAQ-9174 coupled with a NI 9218 module, National Instruments, Austin, TX, USA). The LVDT was put in contact with the motor shaft to be connected to the comb-like structure. The motor shaft displacement was continuously acquired over 30 cycles (sampling rate = 3200 Hz) for some representative combinations (i.e., amplitude = 0.8, 1.2, and 1.6 mm; frequency = 1, 2, and 3 Hz). The recorded displacement signals were conditioned (Butterworth low-pass filter, order 8, cut-off frequency = 10 Hz) and analyzed to evaluate their peak-to-peak amplitude and frequency. Measurements were carried out in triplicate. Finally, the mean percentage errors of the measured amplitude and frequency values with respect to the prescribed nominal values were calculated and expressed as mean ± standard deviation (SD) (Figures S2C–S2E).

### Electrical stimulation module

A computational model was developed with the finite element method (FEM) to investigate the spatial distribution of the electric field within the culture chamber, using the AC/DC module from COMSOL Multiphysics software (version 5.3). The overall 3D geometry of the electrical stimulation module was modelled as six divided, homogeneous sub-domains (the PDMS electrical support, Stainless steel 316 wire, Nitinol wire, Polystyrene (PS) chamber, fibrin-gel, and culture medium volume), each with their respective electrical properties. The values of electrical conductivity ( $\sigma$ ) and relative electric permittivity ( $\epsilon_r$ ) for the components are summarized in Table 1. Characterization of the electrical module (Qi et al., 2011; Pavesi et al., 2014; Tsai et al., 2017; Hogenes et al., 2020; Zimmermann et al., 2020, [onlinelibrary.wiley.com](https://onlinelibrary.wiley.com), [www.engineeringtoolbox.com](http://www.engineeringtoolbox.com)).

A physics-controlled mesh was generated using an extra-fine size (number of elements equal to 818,041, and mesh volume equal to 3114 mm<sup>3</sup>), and the study solution was mesh independent. Stationary study was considered as DC stimulation parameters do not change over time, for which the governing equation solved is:

$$-\nabla(\sigma\nabla V - J_e) = Q_{i,v}$$

where  $V$  is the electric potential,  $\sigma$  is the electric conductivity,  $J_e$  and  $Q_{i,v}$  are an externally generated current density and the local current source, respectively. An electrical insulated boundary condition was applied at all external boundaries of the chamber walls. The Stainless-steel electrode boundary surface was set at 0 V potential (ground electrode) and the Nitinol electrode surface boundary potential at 5 V. All other domains and boundaries were set at 0 V at the beginning of the simulation, to establish an initial resting condition state of the entire system.

Moreover, the electrical characterization was also performed by determining the main parameters of the electrical module by using a custom-made electrical stimulator (Marsano et al., 2016), a known resistor  $R$  (50 Ohm) and an oscilloscope (GSP-830, GW Instek, Taiwan). The characterization was performed at 37°C with the wires of the mechanical modules (serving as electrodes) immersed in high glucose Dulbecco Modified Eagle's Medium (DMEM, Sigma-Aldrich, USA). Rectangular-shape pulses with a duration of 2 ms were imposed with an increasing amplitude (from 1 to 10 V) and increasing frequencies ( $F = 1, 2, 3$ , and 10 Hz) (Figures S2F–S2H). For each pulse, the charge injection measurement and the circuit current were acquired and saved. That balance between the injected and the recovered charge revealed that the main charge transfer mechanism was based on non-faradaic charging/discharging, since the injected charge was almost totally recovered (Tandon et al., 2009).

## Bioreactor culture

### *Bioreactor assembling and sterilization*

Single or partially assembled components of the bioreactor, the independent modules, and the bioreactor frame were sterilized by superficial cleaning using Ethanol solution (70%) for 30 min, and consequent exposure of the single parts to 2-h of UV lights sterilization, under the clean environment of the cell culture hood.

### *ECT generation and culture*

Hydrogel-based ECTs were generated by seeding rat origin cardiac cells in a 100  $\mu$ L fibrin gel solution (25 mg/mL fibrinogen, Sigma-Aldrich, USA, 5 U/mL thrombin, Sigma-Aldrich, USA, 4.4 mM CaCl<sub>2</sub>, Sigma-Aldrich, USA, 0.4 mg/mL tranexamic-acid, Sigma-Aldrich, USA) at the density of  $20 \times 10^6$  cells/mL corresponding to  $2 \times 10^6$  cells. The ECTs were generated by directly casting the cell-based fibrin gel into custom-made  $10 \times 4 \times 1$  mm<sup>3</sup> silicone molds (Dublisil, Dreve Denatmid GmbH, Germany) embedding the two metallic posts of the mechanical stimulation submodule (Figure 1D). ECTs were incubated 20 min at 37°C and 5% CO<sub>2</sub> to allow complete polymerization of the fibrin gels. Afterwards ECTs were removed from the silicone molds, attached to the bioreactor frame and transferred into a sterile 24-well plate. Control cell-laden hydrogels cultured without mechanical stimulation were produced without the embedding of the wires and singularly cultured using flat custom-made PDMS (Sylgard 184 Silicone Elastomer Kit, Ellsworth Adhesives, USA) molds as support (Figure 1E), within standard 24 well-plate. All ECTs were cultured for 8 days (37°C, 95% humidity, 5% CO<sub>2</sub>) with standard culture medium. Tranexamic-acid was supplemented to the culture medium every day at the concentration of 0.4 mg/mL to reduce the fibrin gel degradation (Cholewinski et al., 2009). ECTs were monitored using live-imaging microscope systems during the culture time. ECTs were also generated following the same protocol using hiPSC-CMs. After 8 days of culture, functionality analysis under electrical pacing were performed on ECTs in order to evaluate the biological response.

## ECT assessments

### *Quantitative real-time PCR*

Subsequent to the functionality analysis, ECTs were removed from the bioreactor and were cut in two halves, one of which was frozen at –80°C to consequently perform quantitative real-time PCR (real-time qPCR). After thawing, followed digestion in TRI-Reagent (Sigma-Aldrich, USA) and the mRNA was isolated following standard protocols. In short, superscript III REV transcript 10,000 UN kit (Thermo-Fisher Scientific, USA), was used to reverse-transcript cDNA from mRNA. The program followed for that was: 10 min at 70°C,



10 min at 25°C, followed by 30 min at 48°C and 5 min at 95°C. Real-time qPCR was performed using TaqMan assays master mix (Thermo-Fisher Scientific, USA), using a ABI 7300 RT-PCR cycler (Applied Biosystems, USA). Expression of the most relevant cardiac markers: Connexin 43 (*Gaj1*, Rn01433957\_m1), troponin I (*Tnni3*, Rn00437164\_m1), Myosin light chain2 ventricular (*Myh2*, Rn02769676\_s1), Myosin light chain7 atrial (*Myh7*, Rn01752521\_g1), Myosin heavy chain 7 (*Myh7*, Rn01488777\_g1) and Myosin heavy chain 6 (*Myh6*, Rn00691721\_g1), as well as N-Cadherin (*Cdh2*, Rn00580099\_m1), were investigated. Furthermore, Tenascin C (*Tnc*, Rn01454947\_m1), Collagen type I (*Col1a1*, Rn01463848\_m1) and type III (*Col3a*, Rn01437681\_m1),  $\alpha$ -smooth muscle actin (*Acta2*, Rn01759928\_g1), Matrix Metalloproteinase 9 (*Mmp9*, Rn00579162\_m1) expression were investigated as typical fibrosis tissue markers. mRNA expression was normalized to the value of the glyceraldehyde-3-phosphate dehydrogenase (*Gapdh* Rn01775763\_g1) expression for each tested gene and expressed as the ratio between auxotonic stimulated ECTs and statically cultured ECTs, as well as ratio between auxotonic stimulated ECTs and initial cardiac population embedded in the ECTs. All gene primers were from Thermo-Fisher Scientific (USA). Raw data can be found in [Figure S3](#).

### *Histology and immunofluorescence staining*

Cell distribution, tissue remodeling and organization were evaluated by Hematoxylin and Eosin (H&E, Biosystems, Switzerland) staining on sample slices. ECTs halves not dedicated for qPCR analysis were used for histology and immunofluorescence staining. The tissues were washed with phosphate-buffered saline (PBS, Sigma-Aldrich, USA) and fixed by an overnight treatment with 4% paraformaldehyde (PFA, Sigma-Aldrich, USA). For the H&E staining, sections of 10  $\mu$ m in thickness were cut with a cryostat (Leica Biosystem CM1950, Leica Biosystem, Germany), and stained according to standard protocols. Images were acquired with a Nikon Ti2 inverted microscope (Nikon, Japan). Immunofluorescence analysis was performed in both rat- and human- origin ECTs. The most relevant cardiac markers, such as sarcomeric  $\alpha$ -actinin and F-actin were investigated on rat-origin ECT. Moreover,  $\alpha$ -smooth muscle actin ( $\alpha$ -SMA) marker was used to assess the role and the phenotype of fibroblasts present in the ECT mixed cell population, and the expression of cell proliferation marker (Ki67) was investigated in rat-origin ECTs. Expression of Octamer-binding transcription factor 4 (Oct-4) and Homeobox protein (Nkx2-5), both markers for undifferentiated cells and for precursor cardiac cells, were investigated in human-origin ECTs. In detail, ECTs were divided in two halves, washed with PBS (Sigma-Aldrich, USA) and fixed using 4% PFA (Sigma-Aldrich, USA) in an overnight treatment. Afterwards, the full three-dimensional (3D) immunostaining was executed following a standard protocol. ECT halves were washed with PBS (Sigma-Aldrich, USA), successively they were incubated for 24 h at room temperature in 5% normal goat serum (Sigma-Aldrich, USA) with 0.25% Triton 100X (Sigma-Aldrich, USA) in PBS (Sigma-Aldrich, USA). After washing with PBS, ECTs were incubated for 24 h in the dark with the following primary antibodies: mouse monoclonal anti-sarcomeric  $\alpha$ -actinin (ABCAM9465, Abcam, UK), fluorescently labelled Alexa488 F-actin (A12379, Invitrogen, Thermo-Fisher Scientific, USA), mouse monoclonal IgG2a  $\alpha$ -SMA (A-2547, Sigma-Aldrich, USA), rabbit polyclonal IgG Ki67 (15580, Abcam, UK). ECTs were again gently washed with PBS and consequently incubated in the dark for 24 h with fluorescently labelled Alexa488, Alexa647 and Alexa546 anti-mouse or Alexa546 anti-rabbit secondary antibodies (Life Technologies, Thermo Fisher Scientific, USA). Nuclei were stained using 4',6-diamidino-2-phenylindole (DAPI, Sigma – Aldrich, USA) at 1:40 for 6 h. Incubations were performed at room temperature and antibodies were diluted in PBS 1X with 0.1% bovine serum albumin (BSA, Sigma-Aldrich, USA). Primary antibody dilution was 1:200 while secondary antibodies were diluted 1:300. Images were acquired using 10X and 40X and 60X objective lenses on a Nikon-CSU1 spinning-disk confocal microscope (Nikon, Japan), and subsequently analyzed by using ImageJ software (NIH, USA).

### *Protein quantification and Western blotting*

For protein extraction, ECTs were cut in small pieces and placed in non-denaturing buffer (10% protease inhibitor cocktail in PBS w/o  $\text{Ca}^{2+}/\text{Mg}^{2+}$ , where the protease inhibitor cocktail was prepared by dissolving 1 EDTA-free tablet, Sigma-Aldrich, Roche, 11873580001, in 1 mL of  $\text{H}_2\text{O}$  for molecular biology). They were then mechanically destroyed using steel beads and loading the samples in TissueLyser II machine (Quiagen, Germany) twice at 30 Hz for 2 min and 30 s, at 4°C. Consequently, 1 mL-insulin syringe was used with a needle to mix the protein extract and break possible tissue remnants. The protein extract was then spun down at high speed for 5 min and the surfactant was kept for quantification. Protein quantification was performed for each sample with the Pierce BCA Protein Assay Kit (Thermo Fisher Scientific, USA) and the first step of western blot (WB) technique was set according with the results. The protein extract was diluted with loading buffer (3 parts of protein extract and 1 part of loading buffer ratio) and loaded on TGX gels (Bio-Rad, USA). The TGX gels were placed in the specific tank for the electrophoresis course. Afterwards the gel was placed in the transfer

membrane (Trans-Blot Turbo Transfer System, Bio-Rad, USA), moved on the cassette and run for 7 min at 1.3 A and 25 V. The membrane was consequently blocked using 5% milk (Sigma, USA) for 1 h at room temperature. The membrane was then incubated with primary antibody (1:500 in 5% milk) over-night at 4°C. The day after, secondary antibody was added to the membrane (1:1000 in 5% milk) and it was incubated for 1 h at room temperature. After washing, the membrane was incubated 5 min with chemiluminescent substrate (Thermo Fisher Scientific, USA) and membrane pictures were acquired with the Chemi-Doc reading machine. Images were analyzed using ImageJ software (NIH, USA).

### Electrical functionality

After 8 days of culture, ECT biological response upon an external electrical pacing was evaluated. Metal wires, in which stimulated ECTs were cast, were used as electrodes (Figure 5J) and connected to an external custom-made electrical stimulator (Marsano et al., 2016). Before the pacing test was started, the bioreactor was positioned inside a live-imaging microscope incubator (ZEISS X91, Olympus, Japan) with temperature and oxygen control (Figure 5H) and each well was investigated to observe ECTs spontaneous beating (Figure 5I). Consequently, under microscope observation electrical pulses (2 ms duration, 1 Hz) were imposed beginning from 1 V amplitude and increasing the voltage in order to measure the minimum electrical field able to generate a beating tissue following the pacing (Excitation threshold, ET). For stimulated ECT, the ET values (V/cm) showed in the results graphs were normalized using the value of the electrical field in the center of the ECT (corresponding to 5 V), according to the computational simulation. Statically cultured ECT electrical functionality was instead evaluated using a custom-made chamber, as the model presented by Tandon and colleagues (Tandon et al., 2009). Likewise, ET values (V/cm) were normalized referring to the electrical field's model. The electrical field in the center of the ECT was also here considered for the normalization (corresponding to 3 V). Moreover, the maximum imposed frequency that the tissue can follow during the pacing, the maximum capture rate (MCR), was evaluated for each sample, varying the frequency of the pulses and observing ECT comeback. Videos of ECT under electrical pacing were acquired using 2X, 4X and 10X objective lenses of the microscope (Videos S1 and S2).

### Force measurement

ECT videos acquisition upon electrical stimulation were investigated to evaluate the developed contractile force. From the acquired videos, using 4X and 10X magnification and 33 frames per second, the Nitinol wire deflection due to ECT contraction was tracked and then quantified using the ParticleTracker ImageJ/Fiji Plugin from MOSAIC Group image-processing algorithm, for multiple particle detection and tracking from digital videos (Sbalzarini and Koumoutsakos, 2005). Starting with the measured displacement values and referring to the values obtained from the calibration process, the averaged among the maximum values of the ECT contraction force was derived from 3 to 4 contraction cycles (Video S3).

### Image analysis

At least 9 immunofluorescence staining images for 4 samples (2 for each condition) from 2 independent experiments were acquired using 40X and 60X objective lenses on a Nikon-CSU1 spinning-disk confocal microscope (Nikon, Japan), and subsequently analyzed using ImageJ software (NIH, USA). All the acquired images were processed removing the background and a threshold technique using the "Li dark method" was used to segment sarcomeric  $\alpha$ -actinin -positive entities. With this technique, the percentage of positive area for sarcomeric  $\alpha$ -actinin, as well as the CM length and elongation (expressed as length-width ratio) were quantified. From the same samples, the same analysis was performed distinguishing between two different portions of the stimulated ECTs. CM orientation was also calculated by assessing the angle between the axis corresponding to the direction of mechanical stimulation and the primary axis of the elongated CMs (sarcomeric  $\alpha$ -actinin -positive object). Furthermore, sarcomere length was quantified by calculating the distance between adjacent sarcomere in 30 CMs from 3 stimulated and 3 control ECTs from 3 independent experiments.

### Video analysis

ECT videos acquisition upon electrical stimulation were segmented and post-processed using a custom Matlab code. In short, the processed videos were analyzed using a Digital Image Correlation (DIC) technique implemented in a custom-made Matlab software, in order to evaluate the strain of the beating tissues under electrical pacing.

### TEM analysis

For transmission electron microscopy (TEM), samples were fixed with freshly prepared fixative solution: 2.5% glutaraldehyde (Electron Microscopy Sciences, USA), 2 % paraformaldehyde (Electron Microscopy Sciences, USA), in 0.1 M PIPES buffer (Sigma-Aldrich, USA), overnight at 4°C. The day after, the fixative solution was gently removed and replaced with washing buffer (0.1 M PIPES buffer). The washing step was performed 3 times and for 10 min each time. Samples were then prepared for acquisition with post-fixation in 1% buffered osmium tetroxide (Electron Microscopy Sciences, USA) for 1 h at 4°C, *en-block* staining with Uranyl acetate (Electron Microscopy Sciences, USA) for 1 h at 4°C in the dark, dehydration in graded series of ethanol (30%, 50%, 70%, 96 and 100% vol/vol). Consequently, embedding for sectioning was carried out into 60°C oven for 48 h. semi-thin sections were cut from the embedded block with a glass knife and then thin sections were cut with diamond knives. Sections were observed using a FEI Tecnai T12 Transmission Electron Microscope (FEI, USA) operating at 80 kV and images were recording using a TVIPS F416 CMOS digital camera.

### QUANTIFICATION AND STATISTICAL ANALYSIS

All data are presented as means  $\pm$  Standard Errors of the Mean (SEMs), except for [Figure 2](#), in which data are presented as means  $\pm$  Standard Deviation (SD). The exact values of n are indicated in the corresponding figure legends. For comparison between groups, unpaired Student's t-test ([Figure 5G](#)) or Mann-Whitney U test ([Figures 2B, 2F, 2G, 5A, and S3C–S3F](#)) was used. The equality of probability distributions was assessed using Shapiro-Wilk test. Statistical analyses were conducted using GraphPad Prism 9 ((GraphPad Software, Inc., USA)). Statistical significance was set at  $p < 0.05$ .

In the graphs, statistical significance is denoted as \* for  $p \text{ value} \leq 0.05$ , \*\* for  $p \text{ value} \leq 0.01$ , \*\*\* for  $p \text{ value} \leq 0.001$ , and \*\*\*\* for  $p \text{ value} \leq 0.0001$ , while no-significance is denoted with ns.